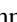








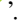
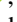




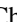






# REQUIEM-2D: A Diversity of Formation Pathways in a Sample of Spatially Resolved Massive Quiescent Galaxies at $z \sim 2$

Mohammad Akhshik<sup>1</sup> , Katherine E. Whitaker<sup>2,3</sup> , Joel Leja<sup>4,5,6</sup> , Johan Richard<sup>7</sup> , Justin S. Spilker<sup>8</sup> , Mimi Song<sup>2</sup> , Gabriel Brammer<sup>3,9</sup> , Rachel Bezanson<sup>10</sup> , Harald Ebeling<sup>11</sup> , Anna R. Gallazzi<sup>12</sup> , Guillaume Mahler<sup>13,14</sup> , Lamiya A. Mowla<sup>15</sup> , Erica J. Nelson<sup>16</sup> , Camilla Pacifici<sup>17</sup> , Keren Sharon<sup>18</sup> , Sune Toft<sup>3,9</sup> , Christina C. Williams<sup>19</sup> , Lillian Wright<sup>2</sup>, and Johannes Zabl<sup>20</sup> 

<sup>1</sup> Department of Physics, University of Connecticut, Storrs, CT 06269, USA; [mohammad.akhshik@uconn.edu](mailto:mohammad.akhshik@uconn.edu)

<sup>2</sup> Department of Astronomy, University of Massachusetts, Amherst, MA 01003, USA

<sup>3</sup> Cosmic Dawn Center (DAWN), Denmark

<sup>4</sup> Department of Astronomy & Astrophysics, The Pennsylvania State University, University Park, PA 16802, USA

<sup>5</sup> Institute for Computational & Data Sciences, The Pennsylvania State University, University Park, PA 16802, USA

<sup>6</sup> Institute for Gravitation and the Cosmos, The Pennsylvania State University, University Park, PA 16802, USA

<sup>7</sup> Univ. Lyon, Univ. Lyon1, Ens. de Lyon, CNRS, Centre de Recherche Astrophysique de Lyon UMR5574, F-69230, Saint-Genis-Laval, France

<sup>8</sup> Department of Physics and Astronomy and George P. and Cynthia Woods Mitchell Institute for Fundamental Physics and Astronomy, Texas A&M University, 4242 TAMU, College Station, TX 77843-4242, USA

<sup>9</sup> Niels Bohr Institute, University of Copenhagen, Jagtvej 128, DK-2200 Copenhagen, Denmark

<sup>10</sup> Department of Physics and Astronomy, University of Pittsburgh, Pittsburgh, PA 15260, USA

<sup>11</sup> Institute for Astronomy, University of Hawaii, 2680 Woodlawn Drive, Honolulu, HI 96822, USA

<sup>12</sup> INAF-Osservatorio Astrofisico di Arcetri, Largo Enrico Fermi 5, I-50125 Firenze, Italy

<sup>13</sup> Institute for Computational Cosmology, Durham University, South Road, Durham DH1 3LE, UK

<sup>14</sup> Centre for Extragalactic Astronomy, Durham University, South Road, Durham DH1 3LE, UK

<sup>15</sup> Dunlap Institute for Astronomy and Astrophysics, University of Toronto, 50 St George Street, Toronto ON, M5S 3H4, Canada

<sup>16</sup> Department of Astrophysical and Planetary Sciences, 391 UCB, University of Colorado, Boulder, CO 80309-0391, USA

<sup>17</sup> Space Telescope Science Institute, 3700 San Martin Drive, Baltimore, MD 21218, USA

<sup>18</sup> Department of Astronomy, University of Michigan, 1085 South University Avenue, Ann Arbor, MI 48109, USA

<sup>19</sup> Steward Observatory, University of Arizona, 933 North Cherry Avenue, Tucson, AZ 85721, USA

<sup>20</sup> Institute for Computational Astrophysics and Department of Astronomy & Physics, Saint Mary's University, 923 Robie Street, Halifax, Nova Scotia, B3H 3C3, Canada

Received 2022 March 2; revised 2022 October 31; accepted 2022 November 28; published 2023 February 7

## Abstract

REQUIEM-2D (Resolving Quiescent Magnified Galaxies with 2D Grism Spectroscopy) comprises a sample of eight massive ( $\log(M_*/M_\odot) > 10.6$ ) strongly lensed quiescent galaxies at  $z \sim 2$ . REQUIEM-2D combines the natural magnification from strong gravitational lensing with the high-spatial-resolution grism spectroscopy of the Hubble Space Telescope through a spectrophotometric fit to study spatially resolved stellar populations. We show that quiescent galaxies in the REQUIEM-2D survey have diverse formation histories with age gradients at the  $1\sigma$ – $3\sigma$  level, including examples of (1) a younger central region supporting outside-in formation, (2) flat age gradients that show evidence for both spatially uniform early formation and inside-out quenching, and (3) regions at a fixed radial distance having different ages (such asymmetries cannot be recovered when averaging stellar population measurements azimuthally). The typical dust attenuation curve for the REQUIEM-2D galaxies is constrained to be steeper than Calzetti's law in the UV and generally consistent with  $A_V < 1$ . Combined together and accounting for the different physical radial distances and formation timescales, we find that the REQUIEM-2D galaxies that formed earlier in the universe exhibit slow and uniform growth in their inner core, whereas the galaxies that formed later have rapid inner growth in their inner core with younger ages than the outskirts. These results challenge the currently accepted paradigm of how massive quiescent galaxies form, where the earliest galaxies are thought to form most rapidly. Significantly larger samples close to the epoch of formation with similar data quality and higher spectral resolution are required to validate this finding.


*Unified Astronomy Thesaurus concepts:* [Galaxy formation \(595\)](#); [Extragalactic astronomy \(506\)](#); [Observational astronomy \(1145\)](#)

## 1. Introduction

One of the key empirical findings in observational extragalactic astronomy is the existence of a star formation main sequence (SFMS) manifesting as a population of galaxies with a relatively tight correlation between their star formation rate (SFR) and stellar mass (e.g., Daddi et al. 2007; Elbaz et al. 2007; Noeske et al. 2007; Whitaker et al. 2012, 2014;

Speagle et al. 2014, see also Figure 1). It is also shown observationally that there is a population of massive galaxies with significantly lower SFR than what is expected from the SFMS, known as quiescent galaxies (e.g., Kriek et al. 2006; Brammer et al. 2009; Muzzin et al. 2013). Understanding the existence of the SFMS (e.g., Kelson 2014) and its outliers is one of the major challenges of extragalactic astronomy.

Spectrophotometric observations, which include UV to far-IR data, are extensively used to study quiescent galaxies at  $z \gtrsim 1$  (e.g., Geier et al. 2013; Whitaker et al. 2013, 2021; Hill et al. 2016; Belli et al. 2017, 2019, 2021; Toft et al. 2017; Abramson et al. 2018; Ebeling et al. 2018; Newman et al. 2018;

 Original content from this work may be used under the terms of the [Creative Commons Attribution 4.0 licence](#). Any further distribution of this work must maintain attribution to the author(s) and the title of the work, journal citation and DOI.

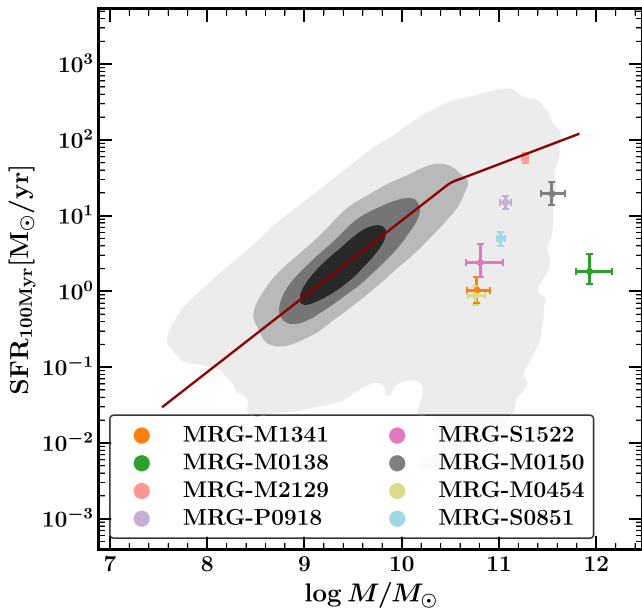


**Figure 1.** SFMS from the 3D-HST survey (Brammer et al. 2012; Momcheva et al. 2016). The stellar populations’ parameters are constrained using *Prospector- $\alpha$*  (Leja et al. 2017, 2020; Johnson et al. 2019). The red line shows the best fit to the SFMS at  $z=1-3$  following Leja et al. (2022) and Whitaker et al. (2014). The REQUIEM-2D galaxies are shown with the circles. For these galaxies, the stellar masses are the total stellar mass formed in all spatial bins and the SFR is sum of the SFRs of individual bins (see Sections 2–4). MRG-M2129 is on the SFMS because it has a dust-obscured star-forming component (see Section 5). Both parameters are corrected assuming a linear gravitational magnification.

Morishita et al. 2018, 2019; Estrada-Carpenter et al. 2019, 2020; Jafariyazani et al. 2020; Setton et al. 2020; Man et al. 2021; Tacchella et al. 2022). These studies imply a diversity among the progenitors, including compact galaxies that form stars centrally (e.g., Williams et al. 2014) and rotationally supported larger star-forming galaxies (e.g., Wisnioski et al. 2015). Quiescent galaxies are thought to form via either “slow” or “fast” channels, leading to different colors, formation timescales, and ages of the stellar populations (e.g., Belli et al. 2019). The cold gas content of quiescent galaxies has also been studied to some extent, revealing a medley of values for the inferred depletion timescales and ratios of gas to stellar mass (e.g., Suess et al. 2017; Spilker et al. 2018; Bezanson et al. 2019; Belli et al. 2021; Man et al. 2021; Whitaker et al. 2021; Williams et al. 2021). These early studies find cases that support fast depletion of the cold gas and/or reduced star formation efficiency associated with the quiescent population.

There is an equally diverse set of potential mechanisms for explaining the existence of quiescent galaxies in cosmological simulations (e.g., Dekel & Birnboim 2006; Tacchella et al. 2015, 2016; Wellons et al. 2015; Zolotov et al. 2015), motivating observational studies in order to constrain the imprints of the corresponding physical processes on their stellar populations. Specifically, constraining the spatial variation of stellar age within the galaxies can shed light on their formation pathways (e.g., Wellons et al. 2015; Tacchella et al. 2016). However, as a stellar population gets older, the variations in the age-sensitive spectrophotometric features decrease, making it very difficult to detect age gradients for an older age baseline. This limits the ideal candidates to “recently”<sup>21</sup> quenched

<sup>21</sup> Roughly defined as galaxies that have not been actively forming stars  $\lesssim 1$  Gyr before observation.

quiescent galaxies, which peak in number density at  $z \gtrsim 1$  (e.g., Cassata et al. 2013).

We present the REQUIEM-2D survey in this paper, studying the stellar populations of quiescent galaxies that cover a range of global ages, stellar masses, and star formation rates (see Akhshik et al. 2020, and Section 2). This survey is designed to use a specific feature of the Hubble Space Telescope (HST) Wide Field Camera 3 (WFC3) grism—its ability to preserve the spatial information perpendicular to the dispersion angle—to study spatially resolved stellar populations. When combining the high spatial resolution of HST with a natural boost from strong gravitational lensing, the REQUIEM-2D survey provides a unique opportunity to constrain the spatially resolved ages and star formation histories of the inner cores of eight massive quiescent lensed galaxies in order to gain further insights into their formation pathways (see also Abramson et al. 2018, for a similar study).

Herein, we present the analyses of the seven targets from the REQUIEM-2D survey; a detailed study of REQUIEM-2D’s pilot target, MRG-S0851, is presented elsewhere (Akhshik et al. 2020, 2021; Caliendo et al. 2021). We summarize the data reduction in Section 2, and present the analysis in Section 3, referring the reader to Akhshik et al. (2020) for a more in-depth discussion of the adopted methodology. We discuss the results in Section 4. In Sections 5 and 6 we discuss the implications of our results. The details of the previously unpublished lensing model for MRG-P0918 are presented in Appendix A.

In this paper, we assume a standard simplified  $\Lambda$ CDM cosmology with  $\Omega_M = 0.3$ ,  $\Omega_\Lambda = 0.7$ , and  $H_0 = 70 \text{ km s}^{-1} \text{ Mpc}^{-1}$  and the Chabrier (2003) initial mass function. All magnitudes are reported in the AB system.

## 2. Data Reduction and Photometric Measurements

### 2.1. Data Reduction

The REQUIEM-2D galaxy survey targets eight strongly lensed quiescent galaxies with redshifts of  $1.6 < z < 2.9$  and demagnified stellar masses of  $10.6 < \log(M_*/M_\odot) < 12$  (see Figures 1 and 2 and also Akhshik et al. 2020, HST-GO-15663; PI: M. Akhshik). The pilot target of the survey, MRG-S0851 (HST-GO-14622; PI: K. E. Whitaker), has been studied in Akhshik et al. (2020, 2021) and Caliendo et al. (2021). Therein, we built and extensively tested our methodology on mock observations as well as the pilot target. We closely follow this methodology to analyze the remaining seven galaxies in this paper:

- 1 MRG-M1341: a highly magnified  $\mu \sim 30$  galaxy at  $z = 1.59$  ( $\mu$  is the linear gravitational magnification; Ebeling et al. 2018; Whitaker et al. 2019; 15 orbits of WFC3/G141),
- 2 MRG-M0138: a very bright, massive galaxy at  $z = 1.95$  with  $H_{F160W} = 17.3$  (Newman et al. 2018; six orbits of WFC3/G141),
- 3 MRG-M2129 and MRG-M0150: massive quenched galaxies at  $z = 2.1$  and  $z = 2.6$  that are rotationally supported and dispersion-dominated, respectively (Newman et al. 2015; Toft et al. 2017; five orbits of WFC3/G141 each),
- 4 MRG-P0918 and MRG-S1522:  $\sim 1$  Gyr old quiescent galaxies at  $z = 2.36$  and  $z = 2.45$  (Newman et al. 2018; seven orbits of WFC3/G141 each),
- 5 MRG-M0454: the most compact galaxy with  $r_{\text{eff}} \sim 0.3$  kpc and the one with the highest redshift,  $z = 2.9$ , in the survey (Man et al. 2021; 12 orbits of WFC3/G141).

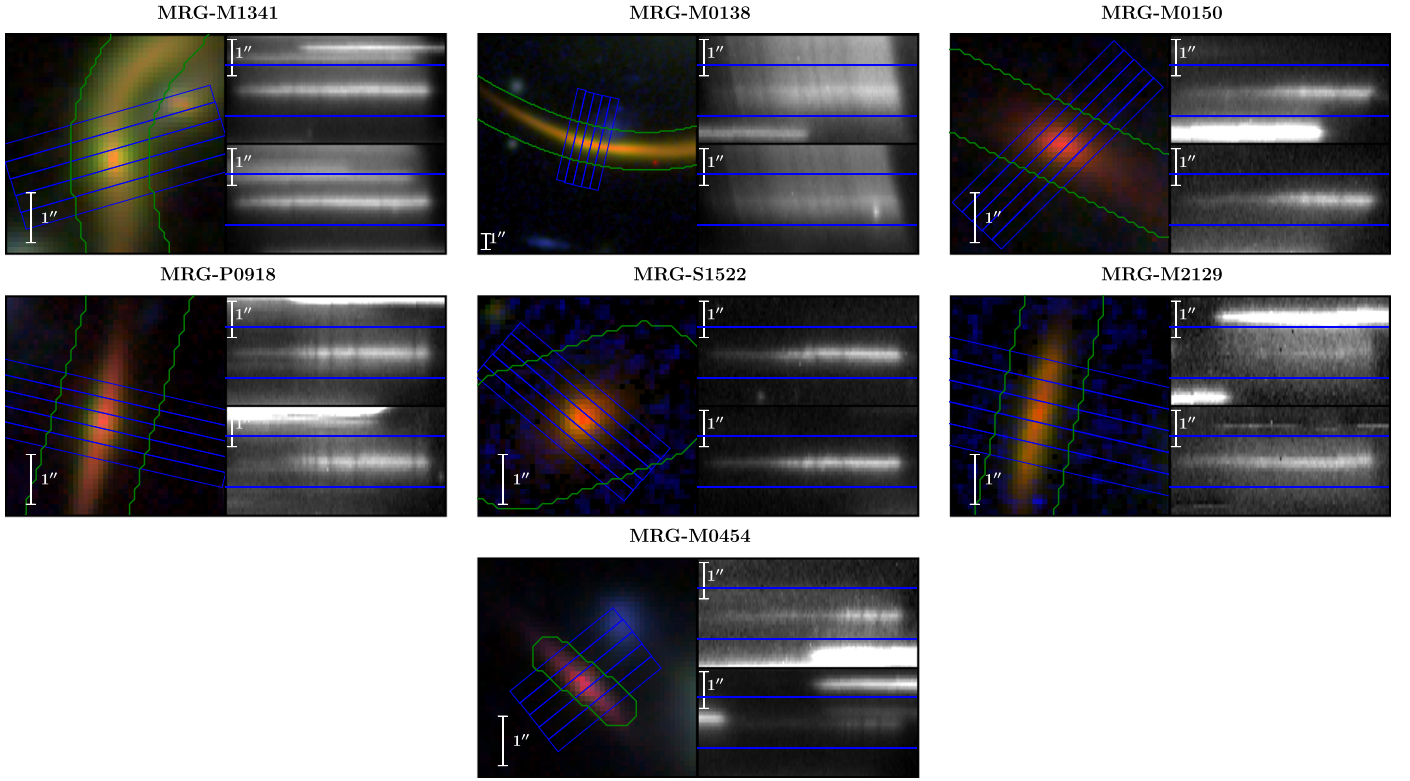


**Figure 2.** Reduced HST observations of the REQUIEM-2D sample. The color images (left) are constructed using  $H_{F160W}$  as red, either  $Y_{F110W}$  or  $J_{F125W}$  as green, and  $U_{F390W}$ , or  $I_{F814W}$  or  $V_{F555W}$  as blue. The green contours show one of the flexible banana apertures that we use to measure photometric fluxes. The blue lines in each subpanel on the left define the five central bins used in the spatially resolved analysis. The two subpanels on the right show data for the two grism dispersion angles used to observe each target in order to minimize contamination. The wavelength is increased from left to right. The blue lines in the right subpanels represent the equivalent extent of the five central bins.

**Table 1**

Photometric Measurements of the Total Flux Density ( $F_{\lambda}$  [erg s<sup>-1</sup> cm<sup>-2</sup> Å<sup>-1</sup>]) for each REQUIEM-2D Target Used in Our Study, Including HST WFC3, ACS, and Spitzer IRAC Filters

Filter/Target	MRG-M1341	MRG-M0138	MRG-M0150	MRG-P0918	MRG-S1522	MRG-M2129	MRG-M0454
F336W	×	×	×	×	×	$12 \pm 7 \times 10^{-19}$	×
F390W	×	×	×	×	$7 \pm 4 \times 10^{-19}$	$7 \pm 5 \times 10^{-19}$	×
F555W	×	$4 \pm 2 \times 10^{-18}$	×	$11 \pm 5 \times 10^{-19}$	×	$5 \pm 2 \times 10^{-19}$	$54 \pm 3 \times 10^{-20}$
F606W	$33 \pm 4 \times 10^{-19}$	×	$6 \pm 3 \times 10^{-19}$	×	$10 \pm 2 \times 10^{-19}$	$5 \pm 2 \times 10^{-19}$	×
F775W	×	×	×	×	×	$9 \pm 2 \times 10^{-19}$	$113 \pm 5 \times 10^{-20}$
F814W	$82 \pm 3 \times 10^{-19}$	×	$12 \pm 2 \times 10^{-19}$	$18 \pm 3 \times 10^{-19}$	$12 \pm 3 \times 10^{-19}$	$8 \pm 1 \times 10^{-19}$	$108 \pm 2 \times 10^{-20}$
F850LP	×	×	×	×	×	$11 \pm 2 \times 10^{-19}$	$100 \pm 6 \times 10^{-20}$
F105W	$215 \pm 2 \times 10^{-19}$	$244 \pm 6 \times 10^{-19}$	×	$26 \pm 2 \times 10^{-19}$	$17 \pm 1 \times 10^{-19}$	$157 \pm 9 \times 10^{-20}$	$101 \pm 3 \times 10^{-20}$
F110W	$238 \pm 3 \times 10^{-19}$	$36 \pm 1 \times 10^{-18}$	$201 \pm 10 \times 10^{-20}$	$38 \pm 1 \times 10^{-19}$	$245 \pm 10 \times 10^{-20}$	$258 \pm 8 \times 10^{-20}$	$105 \pm 2 \times 10^{-20}$
F125W	$271 \pm 2 \times 10^{-19}$	$43 \pm 1 \times 10^{-18}$	$234 \pm 9 \times 10^{-20}$	$475 \pm 5 \times 10^{-20}$	$292 \pm 8 \times 10^{-20}$	$328 \pm 7 \times 10^{-20}$	$114 \pm 2 \times 10^{-20}$
F140W	$271 \pm 1 \times 10^{-19}$	$497 \pm 7 \times 10^{-19}$	$403 \pm 7 \times 10^{-20}$	$64 \pm 1 \times 10^{-19}$	$418 \pm 7 \times 10^{-20}$	$416 \pm 6 \times 10^{-20}$	$172 \pm 2 \times 10^{-20}$
F160W	$266 \pm 1 \times 10^{-19}$	$525 \pm 6 \times 10^{-19}$	$548 \pm 7 \times 10^{-20}$	$72 \pm 2 \times 10^{-19}$	$525 \pm 7 \times 10^{-20}$	$425 \pm 5 \times 10^{-20}$	$238 \pm 1 \times 10^{-20}$
IRAC1	$106 \pm 5 \times 10^{-19}$	$34 \pm 1 \times 10^{-18}$	$32 \pm 2 \times 10^{-19}$	$27 \pm 4 \times 10^{-19}$	$22 \pm 1 \times 10^{-19}$	$209 \pm 6 \times 10^{-20}$	$100 \pm 4 \times 10^{-20}$
IRAC2	$68 \pm 2 \times 10^{-19}$	$240 \pm 6 \times 10^{-19}$	$23 \pm 2 \times 10^{-19}$	×	$157 \pm 8 \times 10^{-20}$	$147 \pm 4 \times 10^{-20}$	$69 \pm 3 \times 10^{-20}$

**Notes.** Whenever a filter has not been observed for a target, we denote it by ×. MRG-M2129 also has overlapping F275W and F225W exposures not listed here; it is undetected in these filters with  $1\sigma$  upper limits of  $1.1 \times 10^{-18}$  and  $1.7 \times 10^{-18}$ , respectively<sup>a</sup>. The measured 1.3 mm ALMA  $F_{\lambda}$  flux densities are  $48 \pm 5 \times 10^{-24}$  (MRG-M0138) and  $173 \pm 3 \times 10^{-24}$  (MRG-M2129) in erg s<sup>-1</sup> cm<sup>-2</sup> Å<sup>-1</sup> (Whitaker et al. 2021).

<sup>a</sup> The HST observing programs are GO-14622, PI: Whitaker; GO-15663, PI: Akhshik; GO-15466, PI: Ebeling; GO-13459, PI: Treu; PI: Ebeling; SNAP-14098, PI: Ebeling; SNAP-12884, PI: Ebeling; SNAP-15132, PI: Ebeling; SNAP-11103, PI: Ebeling; GO-12099, PI: Riess; GO-12100, PI: Postman; GO-9722, PI: Ebeling; GO-9292, PI: Ford; GO-10493, PI: Gal-Yam; GO-14496, PI: Newman; GO-14205, PI: Newman; GO-13003, PI: Gladders; GO-11591, PI: Kneib; GO-9836, PI: Ellis.

We use the Mikulski Archive for Space Telescopes (MAST) to access all publicly available HST WFC3 and Advanced Camera for Surveys (ACS) data (see Table 1) along with the REQUIEM-2D Cycle 26 HST program (HST-GO-15663). All HST and Spitzer data are reduced using the “Grism redshift &

line analysis software for space-based slitless spectroscopy,” or Grizli (Brammer 2016). Grizli performs astrometric calibrations of the WFC3-IR and WFC3-UVIS images using the Pan-STARSS catalog (Flewelling et al. 2020) and the Gaia-DR2 catalog (Gaia Collaboration et al. 2018; Lindegren et al.

2018). The final drizzled mosaics are constructed using `AstroDrizzle` (Avila & Hack 2012) with a `pixfrac` of 0.33 and a pixel size of  $0''.1$ .

## 2.2. Constraining Photometric Fluxes and Morphologies

After reducing HST and Spitzer data, we measure photometric fluxes that are major components of our joint spectro-photometric fitting. We first construct HST point-spread functions (PSFs) using `Grizli`. In this step, `Grizli` registers predefined empirical PSFs, retrieved from MAST (Anderson 2016), of each filter for the existing mosaics using the spatial resolution and orientation angles of the contributing exposures. We also construct Spitzer PSFs in a similar way to the HST PSFs. To build our Spitzer PSFs, we first utilize the rich data set in the GOODS-S field and construct the “base” empirical PSFs in each filter on a  $0''.1$  pixel scale. Then, we mimic the visits of the telescope over the REQUIEM fields, building our position-dependent PSFs on a  $5'' \times 5''$  grid, in a box with (a minimum of)  $30''$  on a side around the target.

Using drizzled mosaics and weight maps, we measure the Spitzer and HST photometric fluxes and uncertainties using a methodology combining earlier works by Akhshik et al. (2020), Wuyts et al. (2010), and Skelton et al. (2014). For all targets, we construct a `Galfit` (Peng et al. 2011) model in the  $H_{F160W}$  band for a  $20'' \times 20''$  box around each target, modeling all galaxies that can potentially contaminate our target (for MRG-M0138 the box is  $37''.5 \times 19''$  to accommodate its extended morphology). In each box, we have several light profiles, modeled using different `Galfit` components, and they are used to clean the contamination in all other HST bands after matching the PSF, allowing them to have different overall flux normalizations. We finally use these models to remove the light profiles of all surrounding objects from the images.

Conventional circular-aperture-photometric methods fail to provide a reliable estimate for most targets in the REQUIEM-2D survey due to their extended and somewhat irregular morphologies. We therefore use a variation of “object apertures” following Wuyts et al. (2010): the axis of symmetry is determined by fitting a polynomial function to isophotes of each galaxy, requiring that the distances of opposing points from the axis of symmetry be minimum. We inspect each fit to make sure that the axis of symmetry is satisfactory. Apertures with increasing radii are centered on this axis, defining banana-shaped apertures. These apertures are then used to measure the flux densities (see Figure 2).

It is a standard practice to measure the flux density using a smaller  $0''.7$  diameter aperture and implement a correction factor to total (e.g., Skelton et al. 2014), because using larger apertures does not optimize the signal-to-noise ratio. Thus, we pick an aperture with a radius of  $0''.35\sqrt{\mu}$ , where  $\mu$  is the average linear gravitational magnification of the different images of the galaxy should it be multiply imaged.<sup>22</sup> The aperture correction is then defined to be the ratio of the flux measured using the same aperture with a radius of  $0''.35\sqrt{\mu}$  on the noise-free `Galfit` model to the total flux.

<sup>22</sup> Using smaller apertures is not suitable when the galaxy has color gradients. The radius here is only measuring distances perpendicular to the axis of symmetry, and the full size of the banana aperture is indeed larger (see Figure 2). We also use the average gravitational magnification to avoid making the aperture large perpendicular to the axis of symmetry in the case of extreme magnifications such as MRG-M1341.

To estimate the uncertainties of the HST aperture photometry, we first define a set of empty apertures with increasing radii for the different filters of each target, measuring their fluxes. We then fit a power-law function to the width of the flux distribution and use this scaling relation to estimate the noise following Whitaker et al. (2011). For the Spitzer IRAC channels, we use the square root of the sum of the inverse weight-map pixels as the uncertainty.

The morphology and the lensing models of MRG-M0138, MRG-M2129, MRG-M0150, MRG-M0454, and MRG-M1341 are studied thoroughly in the literature (Umetsu et al. 2014; Zitri et al. 2014; Toft et al. 2017; Newman et al. 2018; Sharon et al. 2020; Zalesky & Ebeling 2020; Jauzac et al. 2021; Man et al. 2021; Rodney et al. 2021). MRG-S1522 has a published lensing model, too (Sharon et al. 2020). The lensing model for MRG-P0918 is presented in Appendix A.

## 3. Spatially Resolved Stellar Populations

We analyze spectrophotometric data using the `requiem2d` code,<sup>23</sup> referring the reader to Akhshik et al. (2020) for more details. The fully Bayesian model is able to constrain the spatially resolved ages and star formation histories (SFHs) of massive distant galaxies using spectrophotometric observations that assume a nonparametric SFH. We choose the grism dispersion direction such that it is perpendicular to the axis of symmetry while also minimizing the contamination from nearby objects. We define seven spatially resolved bins per galaxy using the  $H_{F160W}$  image for our analyses following Akhshik et al. (2020; see Figure 2). Each one of the five central bins is defined to be 3–4 pixels wide in the image plane ( $0''.3$ – $0''.4$ ), noting that this resolution is greater than the FWHM of the PSF of  $0''.18$ . The two outer bins include all of the remaining pixels within the segmentation map on each side.

One important difference between the analyses here and that of Akhshik et al. (2020) is the number of time bins in the nonparametric SFH model, i.e., the lookback time resolution. Akhshik et al. (2020) assume the original FSPS (flexible stellar population synthesis; Conroy et al. 2009; Conroy & Gunn 2010) time resolution ( $\sim 70$  time bins), whereas we find that this approach introduces some artifacts in the recovered SFHs that are produced by different built-in FSPS assumptions. One notable example is the age when `dust1` is added to the model: all stars younger than this timescale, with a default value of  $10^7$  yr, are attenuated by both `dust1` and the usual `dust2` (Conroy & Gunn 2010). It can be shown that at around this timescale, some slight enhancements/depressions manifest themselves in the SFH (e.g., Figure 2 in Akhshik et al. 2021, around 0.01 Gyr). We explicitly check this effect for MRG-P0918 by changing this timescale from 0.01 to 0.015 and 0.02 Gyr and refit the model. The artifacts move in a consistent manner, appearing at the assumed `dust1` timescale. To avoid adding artifacts into the recovered SFH, we instead define 20 time bins for all samples in the model.<sup>24</sup> We note, however, that the `requiem2d` code is fully capable of fitting the finest lookback time resolution ( $\sim 70$ – $90$  bins) produced by FSPS if required.

For those targets with Atacama Large Millimeter/submillimeter Array (ALMA) 1.3 mm detections, MRG-M0138 and

<sup>23</sup> Publicly available at <https://github.com/makhshik/requiem2d>.

<sup>24</sup> These features are small in the sense that we do not see any difference in the inferred parameters of interest such as stellar mass, age, and specific star formation rate by changing the `dust1` timescale.

MRG-M2129, we carefully examine the distribution of the dust continuum emission. In both sources, the dust emission is unresolved in the  $\sim 1-1''.5$  ALMA data (Whitaker et al. 2021). While this resolution is significantly coarser than our spatially resolved bins, the fact that the emission is pointlike implies that there is some information about the spatial distribution of the 1.3 mm flux in the existing data. We performed a number of tests to determine the level of dust emission in each resolved bin that would be consistent with the existing ALMA data, jointly fitting for the 1.3 mm flux density of a series of unresolved point sources with positions fixed to the centers of each of our resolved bins. This analysis suggests that for both MRG-M0138 and MRG-M2129, the 1.3 mm emission is associated with the three central bins, though the distribution of flux among these bins is essentially unconstrained. In other words, the existing ALMA data constrain the total dust emission in these sources and localize it to the central three bins in each source. Therefore, in our fitting procedure we sum the predicted 1.3 mm flux density of the central three bins and compare this to the observed 1.3 mm emission, while for the exterior bins we use only upper limits on the millimeter flux. We implement the ALMA semi-resolved flux in the Bayesian model using the integrated likelihood (e.g., Section 4.3 of Stan Development Team 2020); i.e., for those bins with only an upper limit detection, the integral of the flux likelihood up to that upper limit is included in the Bayesian fitting. For other targets that are undetected in ALMA 1.3 mm, we can in principle use the upper limit, but as these targets are not particularly dusty (see Figures 5(a), (c)–(e), (g), and (h)), adding the upper limit would not be additionally constraining.

We use the Noll et al. (2009) parameterization for dust, assuming a Kriek & Conroy (2013) dust model (e.g., Akhshik et al. 2020). The dust model has three main parameters: (1) `dust1`, which describes the extra attenuation for stars younger than  $10^7$  yr, (2) `dust2`, describing the attenuation for stars older than  $10^7$  yr, and (3) `dust_index`, which is the index of the power-law correction of the attenuation curve.

For each target we perform a separate stellar population fit using `Prospector- $\alpha$`  (Leja et al. 2017; Johnson et al. 2019) to the semi-resolved photometric data, and subsequently use these posteriors in the joint spectrophotometric fit (Akhshik et al. 2020). We divide the metallicity and `dust2` posterior (its  $3\sigma$  width) into 16 boxes, generating a series of FSPS templates for each box (Akhshik et al. 2020). By refitting the weight of each box along with the SFHs using `requiem2d`, we practically use these `Prospector- $\alpha$`  posteriors as weakly informative priors, and we do not expect this choice of priors affect our age estimates (see Figure 15 in Akhshik et al. 2020, for an example of starting from a different `Prospector- $\alpha$`  posterior). We adopt a slightly different approach to model MRG-M2129 and MRG-M0138. Because of the ALMA detections, we have nontrivial `Prospector- $\alpha$`  posteriors for the dust emission parameters (`duste_umin`, `duste_qpah`, `duste_gamma` in FSPS) along with `dust2` and metallicity. We therefore perform a principal component analysis for the full `Prospector- $\alpha$`  posteriors and use two first principal components instead of `dust2` and metallicity to generate more representative FSPS templates. We also allow the dust attenuation curve to be fit separately, to ensure that the model is flexible enough to deviate from the `Prospector- $\alpha$`  posterior to fit the spectrophotometric data. This step is

implemented by defining half-normally distributed hyperparameters, and using them as the standard deviations of the log-normally and normally distributed priors for `dust1`, `dust2`, and `dust_index`. Each one of these priors is centered at the corresponding mean value in each of the 16 boxes and they are used to generate the attenuation curve.

The No-U-Turn Sampler (NUTS; Homan & Gelman 2014), which is wrapped in `pymc3` (Salvatier et al. 2016), is used to sample the full posterior. We generate two Monte Carlo chains, drawing 2000 samples from the posterior in each one (with the exception of older galaxies, MRG-M0138 and MRG-M1341, where we draw 3000 samples for each chain). We discard the first half of each chain as the burn-in phase and compare the two chains to check for divergences using  $\hat{R}$  (Gelman & Rubin 1992). After ensuring convergence, the two chains are combined to construct a total of 2000 draws from the posteriors (3000 for MRG-M0138 and MRG-M1341). Age gradients are defined as the difference between the age of the center and the age of the corresponding bin. Unless stated otherwise, all ages are median ages,  $t_{50}$ , formally defined as  $0.5 = \int_0^{t_{50}} dt' \text{SFR}(t') / \int_0^{t_0} dt' \text{SFR}(t')$  with the integral taken over time (not lookback time) and  $t_0$  as the time of observation.

#### 4. Results

The `requiem2d` code provides the posterior of different parameters as well as the posterior predictive distributions. We show the spectral energy distributions (SEDs), the 1D collapsed grism spectra, and the posterior predictive distributions of each REQUIEM-2D target in Figure 3 here and Figures 9–14 in Appendix C.

The SED fit to the REQUIEM-2D sample is shown in the left panels of Figures 3 and 9–14. We include the Spitzer IRAC channels 1 and 2 as constraints by imposing likelihoods for the global fluxes that are normally distributed with the observed global values and their uncertainties as means and standard deviations, and they are modeled by the summed fluxes of the individual bins. In other words, these data points are not spatially resolved like the HST photometric bands. We therefore denote their corresponding wavelength ranges with a gray shade in the SED plots.

The right panels of Figures 3 and 9–14 show the 1D collapsed spectra of the five central bins for each target, extracted following Horne (1986). While we fit the two outer bins for all targets, the fit is not as reliable because of the fainter wings of the galaxy and/or contamination by nearby sources (e.g., Akhshik et al. 2020, also see Figure 2). We therefore do not consider the outer bins when analyzing the radially varying trends.

Despite a careful selection of the grism dispersion angles, it is impossible to fully remove the contamination from the outer, fainter wings of these galaxies because the targets are dispersed perpendicular to their longer axis of symmetry and are also located in crowded clusters. Therefore, contamination from nearby sources in WFC3/G141 grism data remains significant for three targets: MRG-P0918, MRG-S1522, and MRG-M0454. We show the collapsed 1D spectrum of the contamination in green. The contamination is modeled and removed before fitting following Akhshik et al. (2020), but this procedure is not perfect and therefore the shape of the 1D collapsed spectra is affected to some extent for the mentioned targets (Figures 11, 12, and 14, right panels). However, these

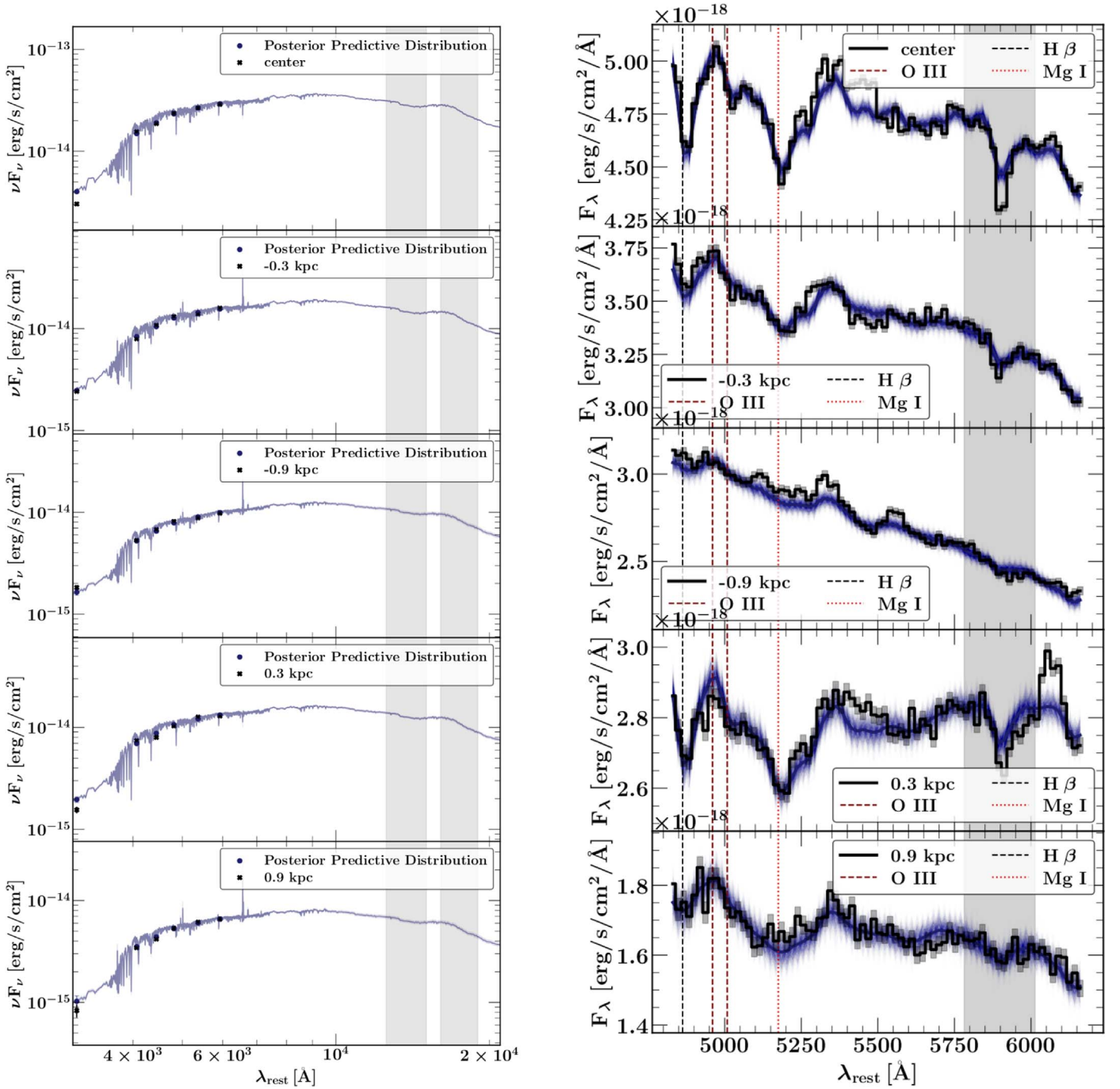


**Figure 3.** Left: the SED of MRG-M1341. The blue line shows 200 draws from the FSPS model. The shaded regions in the SED coincide with the bandpasses of the unresolved Spitzer IRAC channels 1 and 2. Right: the resolved extracted 1D grism spectra. The shaded region ( $1.50\text{--}1.56\ \mu\text{m}$  in the observed frame) in spectra is the Na D line, which is masked in our fitting.

irregularities in the shape of spectra are modeled by fitting the polynomial along with the FSPS model (with reduced  $\chi^2$  values of 0.8–1) to ensure that they do not affect the estimated ages. We finally note that the full `requiem2d` model is constructed and fit in the native 2D space of the WFC3/G141 spectra whereas the 1D collapsed spectra are constructed only for visual purposes.

For each target, we denote the important absorption lines that drive the age and SFH fit using vertical lines. One notable exception is the Na D absorption line in MRG-M1341 (Figure 3). We mask this line since it seems that the stellar absorption cannot fully explain its strength, especially at the

center, potentially implying further absorption by the interstellar medium. This is consistent with earlier observations of the Na D line in MRG-M0138 (Jafariyazani et al. 2020).<sup>25</sup> The masked region is shown with a shaded gray box in Figure 3, right panel; the spectral model in this shaded box is not a fit but is rather an extrapolation. The tension between the data and the best-fit model clearly demonstrates that the stellar absorption

<sup>25</sup> The Na D line for MRG-M0138 is outside the wavelength coverage of WFC3/G141.

assumed for the rest of the model cannot fully explain the Na D strength.

The distances reported in Figures 3 and 9–14 are measured simply by finding the distance between the centers of corresponding adjacent bin in arcseconds. This distance is then translated into physical units using the standard cosmology, and finally it is divided by  $\sqrt{\mu}$  to estimate the source-plane distance. The linear magnification is fairly uniform for all of the targets. We also calculate the distance where half of the total flux is enclosed (see Table 4 for the measured values and their uncertainties) when moving along the axis of symmetry (see Section 2.2) while adding all flux in the perpendicular direction. Distance denoted by  $r_c$  is our preferred distance instead of the usual half-light radius,  $r_{\text{eff}}$ , because it better represents our image-plane bins, which are in turn defined according to the grism observational constraints (Akshshik et al. 2020). MRG-S0815 results are from Akshshik et al. (2020) and are added for completeness. We nevertheless note that the values of  $r_c$  are consistent within the uncertainties with the published half-light radii (Newman et al. 2018; Man et al. 2021), justifying this decision. We also use the term “inner core” to refer to  $r < r_c$ .

We show the specific star formation rate of the five central bins for each target in Figure 4 and the gradients of the different stellar population parameters in Figure 5. Figure 5 displays the values at the redshift of observation. We can identify three different categories of galaxies based on the detected age gradient patterns when noting the difference in the physical distances: (1) younger in the center, (2) flat, and (3) non-axisymmetric gradients. We choose mass-weighted age as the important parameter because it summarizes the average behavior of the SFH. Also, it is suggested that age gradients can be connected to the mechanisms of the formation pathways of the galaxies (e.g., Wellons et al. 2015). In the following section, we synthesize the results from the REQUIEM sample and discuss in the context of our current understanding of formation and quenching pathways for quenched galaxies.

## 5. Discussion

The goal of the REQUIEM-2D survey is to measure age and SFH gradients for the eight lensed quiescent galaxies through a spectrophotometric fit. We discuss our fitting algorithm in the preceding sections, and here we present and discuss the implications of the measured gradients in the stellar populations.

MRG-S1522 is the only galaxy in the REQUIEM-2D sample that is clearly younger in the inner core ( $r/r_c \lesssim 1$ ; Figure 5(e)). Its SFH in Figure 4(e) reveals that the central bin remains more star-forming than the outer bins between lookback times of  $\sim 300$  Myr and  $\sim 1$  Gyr, explaining the younger age at the center. Overall, this galaxy is consistent with an outside-in formation.

Both MRG-M0138 and MRG-M1341 have flat age gradients in the inner core (Figures 5(a) and (b)). Even though the age gradients have similar patterns, Figures 4(a) and (b) reveal different SFHs. The SFH of MRG-M0138 remains roughly the same across the galaxy with an insignificant dip in sSFR at the center at lookback times of 300–500 Myr, whereas the SFH in MRG-M1341 is different at lookback times of  $\sim 10$  Myr to  $\sim 200$  Myr, i.e., the outer bins continue forming stars relative to the quenching center. Quenching in MRG-M1341 may therefore have proceeded inside out (e.g., Wellons et al. 2015;

Nelson et al. 2021), unlike the uniform quenching in MRG-M0138. As the dominant fraction of the stellar mass in MRG-M1341 is formed much earlier in the universe (lookback times  $>1$  Gyr) at similar rates across the galaxy, the median age does not show a statistically significant gradient.<sup>26</sup>

The age gradients in MRG-M0454, MRG-M2129, MRG-P0918, and MRG-M0150 are all mildly non-axisymmetric at  $\sim 1\sigma$  level,<sup>27</sup> with one side of the galaxy older than the other side at similar distances. We report z-scores<sup>28</sup> of the age differences between the two outermost bins being 1.5, 1.3, 1.0, and 0.6, respectively (see Figures 5(c), (d), (f), and (g)). This could indicate that a merger or interaction with another galaxy played a role in their formation. For three galaxies, MRG-M0150, MRG-M0454, and MRG-P0918, the SFH on one side dips below the SFH on the other side for lookback times of  $\sim 100$  Myr to  $\sim 1$  Gyr, leading to an older age. The asymmetrical features are not uncommon in spatially resolved studies of quiescent galaxies (e.g., Figure 8 in Li et al. 2015; Figure 4 in Setton et al. 2020). However, this non-axisymmetric trend vanishes if we azimuthally combine the data points given their distances from the center, consistent with Setton et al. (2020).

The non-axisymmetric age gradient in MRG-M2129 (Figure 5(f)) is caused by the centrally concentrated 1.3 mm ALMA flux. One bin remains star-forming all along in MRG-M2129 in order to produce the significant measured 1.3 mm flux. It is interesting that this feature does not exist in the one other galaxy with a 1.3 mm ALMA detection in the REQUIEM-2D sample (MRG-M0138). This is likely because the ratio of the ALMA flux to the flux at other wavelengths such as  $H_{\text{F160W}}$  is significantly smaller than that in MRG-M2129. The ALMA detection can be roughly attributed to the three central bins. The fitting itself prefers the adjacent bin to the central bin as the dominant producer of the ALMA flux in MRG-M2129. We fit another model assuming that 1.3 mm ALMA flux can only be attributed to the central bin, and the resulting SFH changed to significant star formation at the center. As the ALMA beam size is  $\sim 1''.5 \times 1''.1$  (Whitaker et al. 2021), we cannot distinguish between these two cases. We therefore caution that the age gradient pattern in MRG-M2129 is largely affected by the assumption for the spatial location of the 1.3 mm ALMA detection. The ALMA detection also leads to a different pattern of SFR gradients to that in Toft et al. (2017).

With the exception of MRG-M0138,<sup>29</sup> we measure metallicities consistent with subsolar to solar for all of our targets, broadly in agreement with previous measurements (Toft et al. 2017; Newman et al. 2018; Jafariyazani et al. 2020; Man et al. 2021). While we do not detect any stellar metallicity gradients, there are slight hints of a relatively metal-rich center for

<sup>26</sup> A careful observer, however, notices that the average median age is lower in the outskirts, which is consistent with the SFH pattern even if it is not statistically significant.

<sup>27</sup> That is, this non-axisymmetric trend is washed away upon azimuthally combining the data points and we only have a flat age gradient.

<sup>28</sup> In this paper, “z-scores” are calculated using the age difference posterior by dividing the median by the  $1\sigma$  width of the distribution. We note that no assumption is made about the statistical independence of the age uncertainties among different bins, as the full posteriors of the age differences are used. In our analyses, z-scores indicate how many standard deviations the age differences are from zero.

<sup>29</sup> We find a supersolar metallicity for this target, also consistent with Jafariyazani et al. (2020) and Newman et al. (2018).

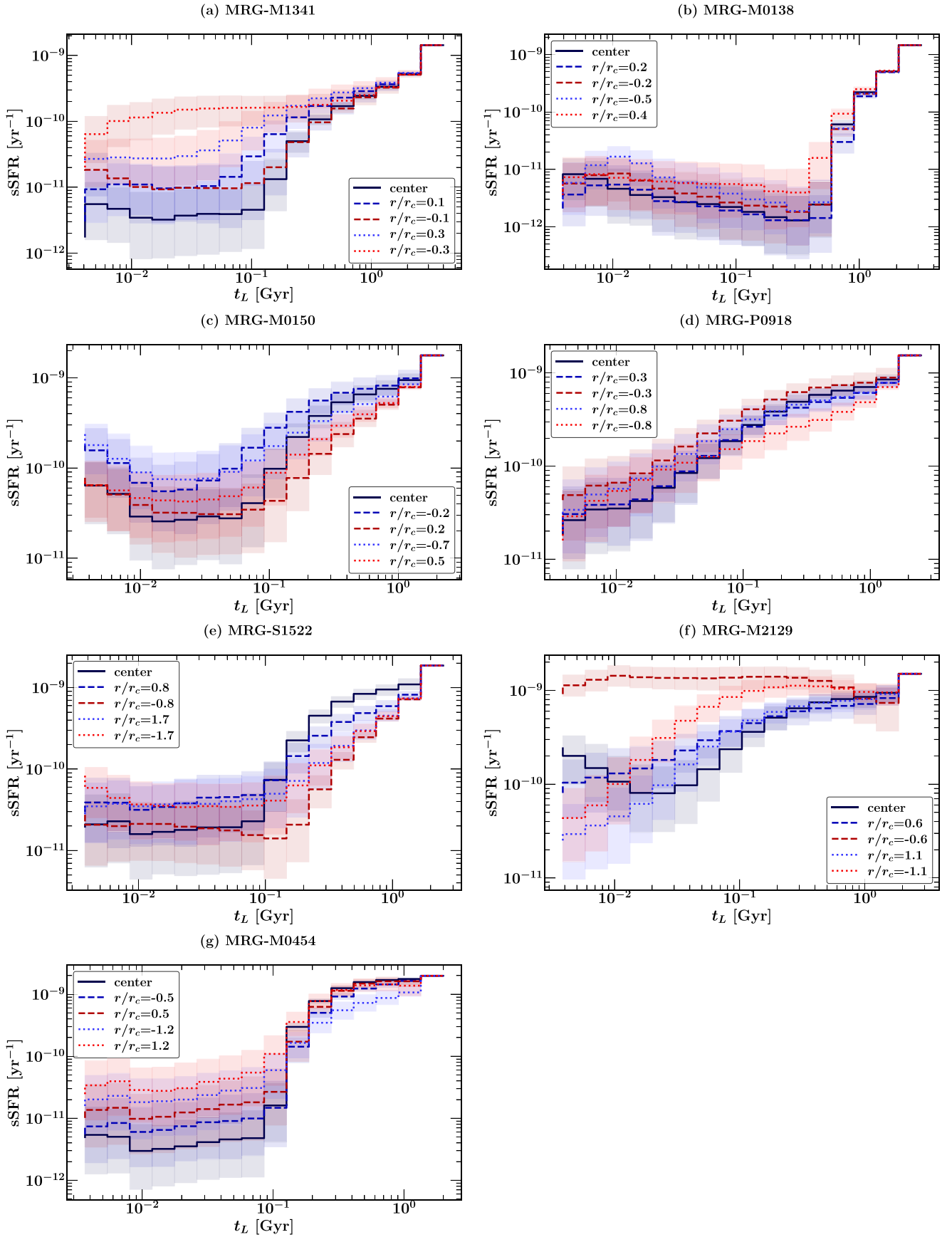


**Figure 4.** Evolution of the specific star formation rate of REQUIEM-2D galaxies.  $r/r_c$  indicates the bin's distance from the center normalized to the distance that encloses half of the light (see the text, Section 4 and Table 4)



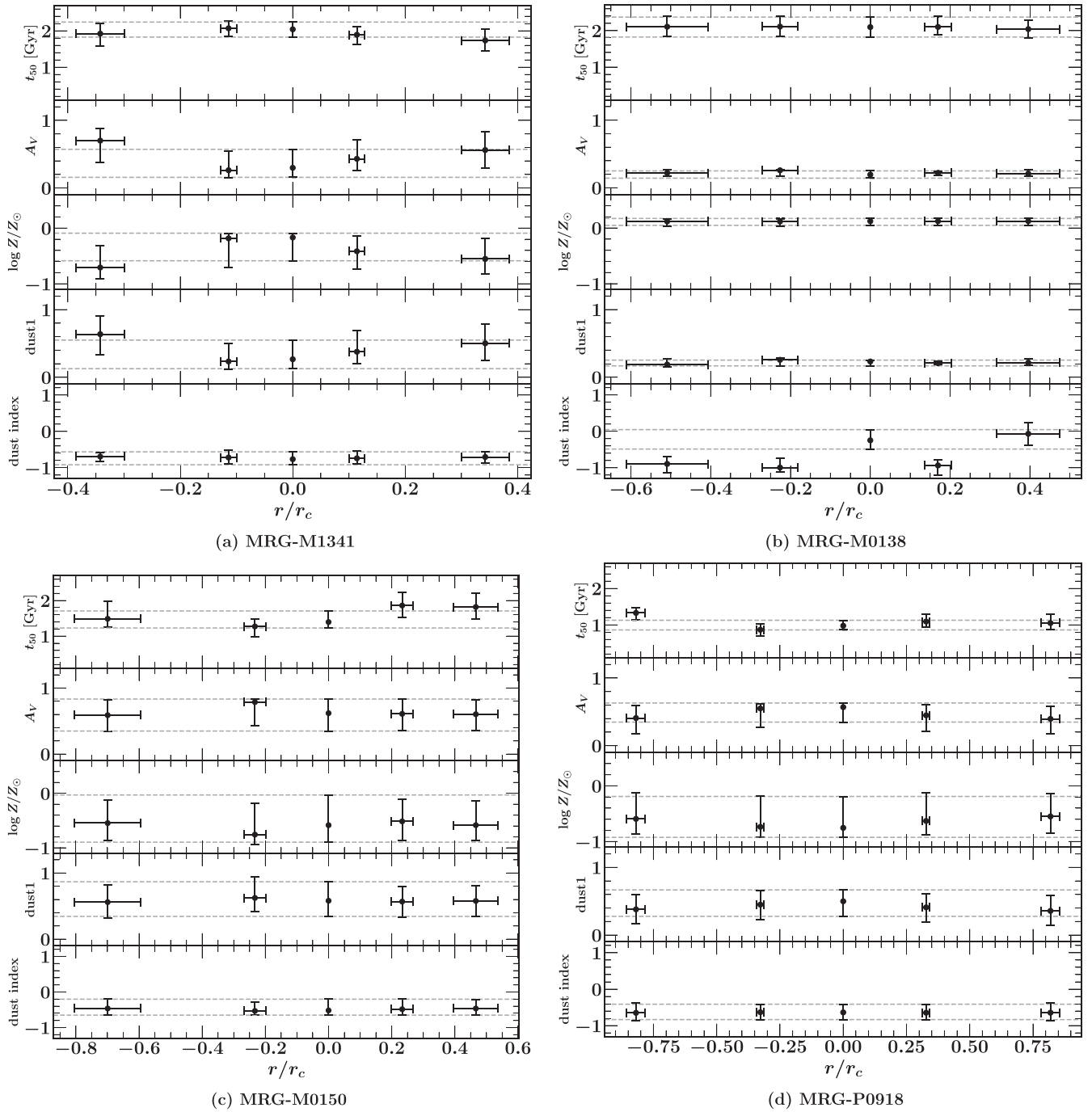


**Figure 5.** Parameters of different stellar populations at the observing redshift. The dashed line shows the  $1\sigma$  width of the uncertainty for the central bin, added to assist in identifying potential gradients.  $r/r_c$  indicates the bin’s distance from the center normalized to the distance that encloses half of the light (see the text, Section 4 and Table 4). MRG-S0815 results are from Akhshik et al. (2020) and are added for completeness.

MRG-M0454 and MRG-M1341 (Figures 5(a) and (g)), but our measurements are not statistically significant.

Taken at face value, the measured flat metallicity gradient in MRG-M0138 in Figure 5(b) is consistent with Jafariyazani et al. (2020). However, for the flat metallicity gradients in other targets, we note an important caveat. WFC3/G141 has a lower spectral resolution than the ground-based spectroscopic measurements with instruments such as Keck/MOSFIRE, which may not help with constraining potential metallicity gradients, given the estimated metallicity uncertainties here ( $\sim 0.3$ – $0.5$  dex). These uncertainties of several orders of magnitude are consistent with similar studies (e.g., Estrada-Carpenter et al. 2019). For all

targets, we use the same priors for dust and metallicity for all bins, and for half of the targets (MRG-P0918, MRG-M0150, MRG-M1341, and MRG-S1522) we get a metallicity posterior consistent with our flat prior. Therefore, our measurements cannot conclusively reject flat metallicity gradients for the REQUIEM-2D targets. Future measurements with the James Webb Space Telescope (for example with the NIRSpect/integral field unit (IFU)) should be suitable to answer this important question.

We find that the median stellar masses of the REQUIEM-2D galaxies (Figure 1) are  $\sim 0.1$ – $0.5$  dex higher than those previously published by Man et al. (2021) and Newman

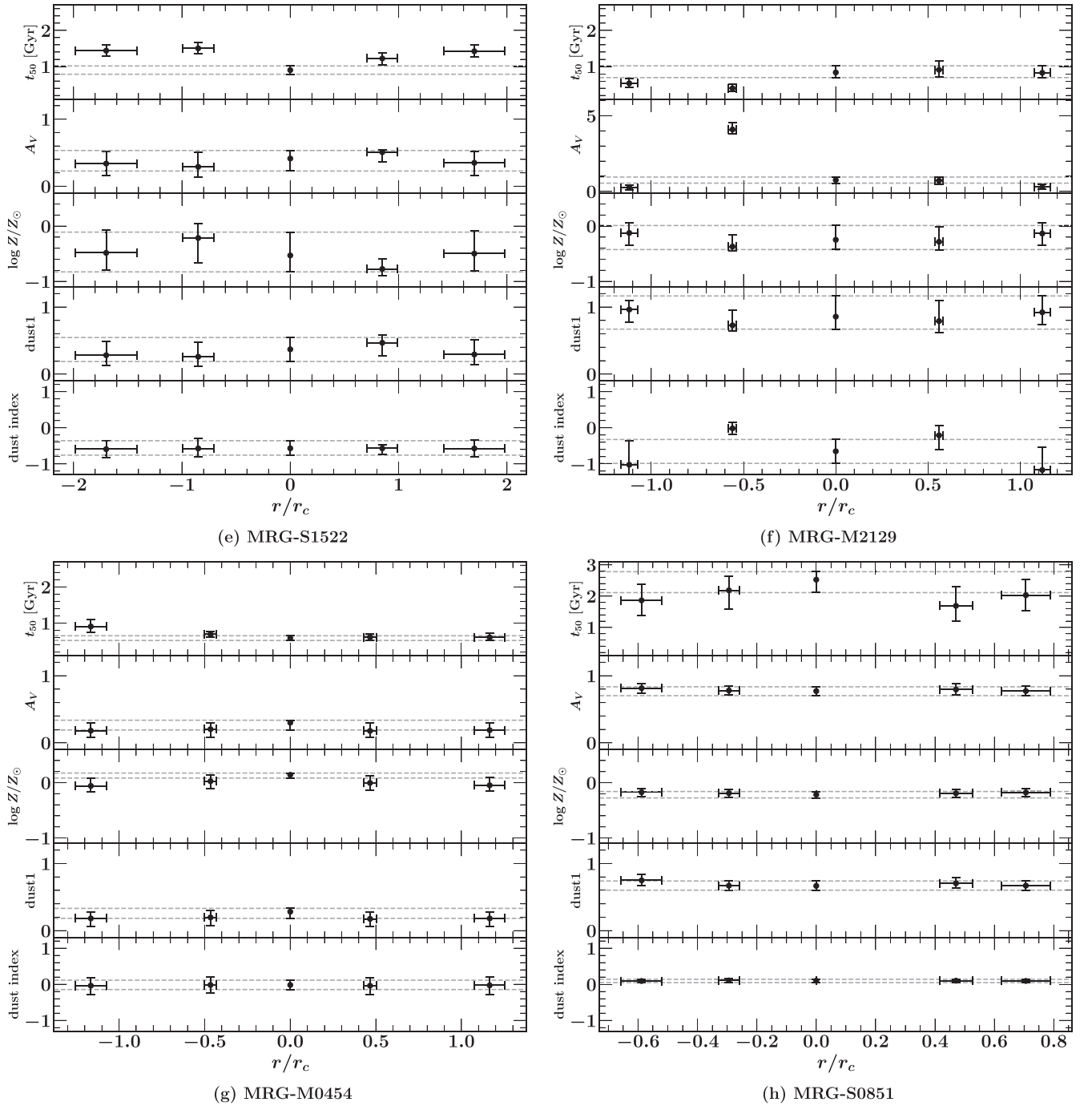
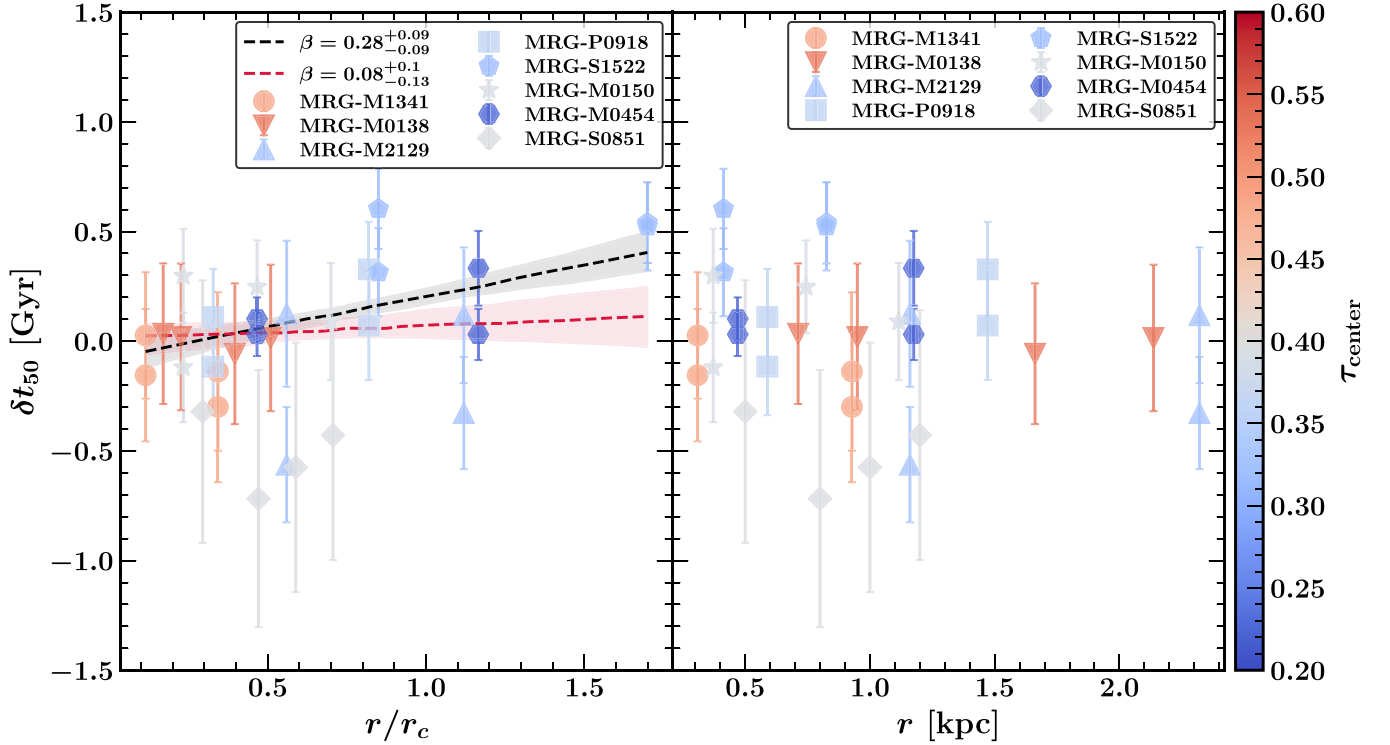


Figure 5. (Continued.)

et al. (2018) for most targets, although for some targets these measurements are consistent within the  $1\sigma$  uncertainties. This offset can be partially explained by the fact that we use nonparametric SFHs, unlike Man et al. (2021) and Newman et al. (2018), and this leads to higher stellar masses and older ages (e.g., Leja et al. 2019). However, the most extreme offset of  $\sim 0.5$  dex in MRG-M1341 is also related to an offset in the HST photometry. We use banana-shaped apertures (Section 2.2) that efficiently enclose fluxes even for unconventional morphologies such as that of MRG-M1341 (Figure 2, top left panel), whereas Source Extractor (Bertin & Arnouts 1996) and slit-shaped apertures are used in Man et al.

(2021) and Newman et al. (2018). Therefore, we measure higher fluxes for some targets in general, leading to higher stellar masses in our SED fits. Specifically, our measured magnitude for MRG-M1341 in HST WFC3/F140W band is  $\sim 0.2$  dex lower (brighter).

We find  $\text{dust\_index} < 0$  for the majority of targets and  $A_V < 1$ , consistent with earlier studies of low-redshift galaxies (e.g., Salim et al. 2018). A negative  $\text{dust\_index}$  corresponds to a steeper attenuation curve than the Calzetti et al. (2000) law, leading to more UV attenuation and less IR attenuation comparably (Kriek & Conroy 2013). We do not detect gradients in either of these dust parameters for the majority



**Figure 6.** Measured spatially-resolved age differences for the REQUIEM-2D galaxies vs. the distance and normalized distances to the half-light radii.  $\delta t_{50}$  is the difference between the age of the corresponding bin and age of the center for each target in gigayears, i.e.,  $\delta t_{50} = t_{\text{spatial bin}} - t_{\text{center}}$ , and the median age,  $t_{50}$ , is defined to be  $0.5 = \int_0^{t_{50}} dt \text{SFR}(t) / \int_0^{t_0} dt \text{SFR}(t)$ , where  $t_0$  is the observing lookback time.  $r_c$  denotes the half-light radius, and the black dashed line and shaded region are the best fit and the  $1\sigma$  width of the linear fit to all data points. The red dashed line is the same fit excluding data points for MRG-S1522, which is the only target showing a significant age difference beyond the half-light radius.  $\beta$  denotes the slope of the linear fit and its  $1\sigma$  posterior uncertainty with a prior of  $\beta \sim \mathcal{N}(0, 100)$ . Data points are color-coded with the quenching timescale of the central bin, defined following Carnall et al. (2018).

of our sample. The only exceptions are MRG-M0138 and MRG-M2129 (Figures 5(b) and (f)), both having a centrally concentrated 1.3 mm ALMA detection.  $A_V$  is only greater than 1 magnitude for the central region of MRG-M2129, which appears to host a dust-obscured star-forming region, producing the significant observed 1.3 mm ALMA flux. It is perhaps surprising that one data point can have such a significant impact on the fit. This will be explored in more detail in a future paper (R. Popescu et al. 2022, in preparation).

We are able to constrain the ages and the SFHs of the REQUIEM-2D galaxies at different physical radii thanks to the morphological diversity of the targets. The variation of the magnification-corrected physical distances across the galaxies can be used to combine the age gradients for the full sample. In Figure 6, we combine the measured age gradients relative to the center for the REQUIEM-2D galaxies as a function of radial distances normalized using their half-light radii,  $r_c$  (see Section 4, for the exact definition). We color-code the age differences using the quenching timescale,  $\tau_{\text{center}}$ , defined following Carnall et al. (2018).<sup>30</sup> The age difference,  $\delta t_{50}$ , is defined to be the difference between the age of a given bin and the age of the central bin for each target in gigayears. It is evident that most measured age differences for the REQUIEM-2D galaxies are only sampling the inner core,  $r < r_c$ , and are consistent with 0, i.e., a flat age gradient. However, when we consider measurements at  $r \gtrsim r_c$ , especially for MRG-S1522,

there seems to be an upward trend. We perform two separate linear fits to the REQUIEM-2D age gradients with and without MRG-S1522. Only when including MRG-S1522 do we have a statistically significant positive slope. So while the combined age gradients for the REQUIEM-2D sample seem to be consistent with younger stellar populations in the inner core, this effect is driven by a single galaxy. To robustly confirm such a conclusion, a larger sample with more independent data points at or beyond the half-light radius is required.

We find a correlation between the quenching timescale at the center,  $\tau_{\text{center}}$ , and the age gradient patterns presented in Figure 6. The REQUIEM-2D galaxies that have smaller  $\tau_{\text{center}}$ , that is their cores are forming fast, also have a younger stellar population in their inner core than in their outskirts. Conversely, those galaxies that form their inner cores slowly also do so in a uniform manner, as they have flat age gradients at  $r < r_c$ .

To further investigate this correlation in Figure 6, we plot the quenching timescale at the center versus the global formation timescale  $t(t_{50})/t_{\text{univ}}$  (i.e., the ratio of the age of the universe when 50% of the total stellar mass formed to the age of the universe at observation) in Figure 7. Small values for this ratio of formation timescale represent galaxies that have already formed half of their stellar mass early in the universe, whereas larger values represent those that form later. Interestingly, galaxies that form their cores faster (low  $\tau_{\text{center}}$ ) also seem to form later in the universe (high  $t(t_{50})/t_{\text{univ}}$ ) and vice versa. We therefore conclude that the REQUIEM-2D galaxies that are formed earlier in the universe are also forming their inner cores slowly and uniformly, whereas the galaxies in our sample that

<sup>30</sup>  $\tau = [t(t_{\text{quench}}) - t(t_{50})]/t(t_{\text{quench}})$  where  $t_{\text{quench}}$  and  $t_{50}$  are the lookback times when the normalized SFR/SFR = 0.1 and 50% of the stellar mass is formed, respectively.  $t(t_L) = t(z_{\text{obs}}) - t_L$ , that is the age of the universe at lookback time  $t_L$  if the galaxy is observed at redshift  $z_{\text{obs}}$ .

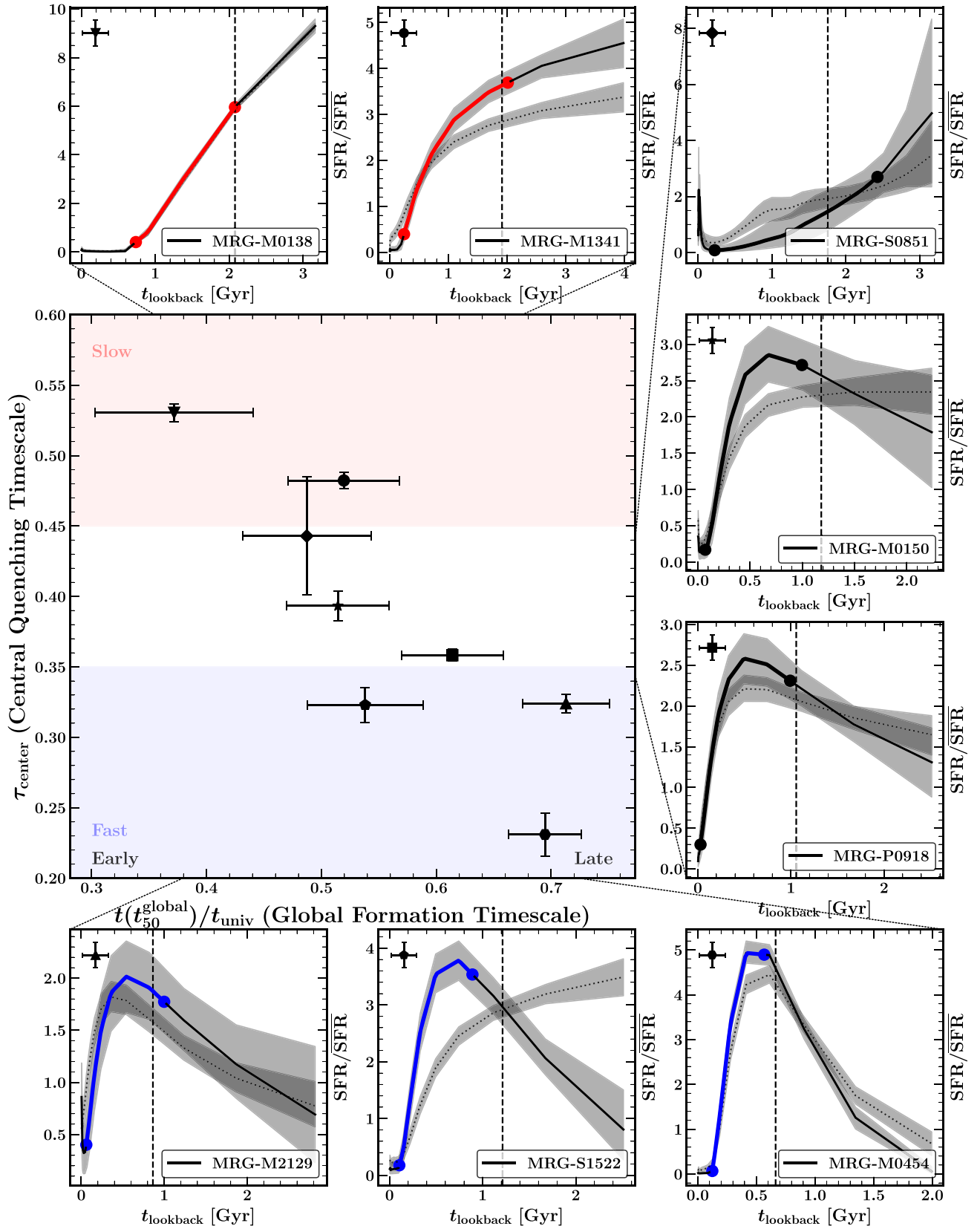


**Figure 7.** The quenching timescale of the central bin, defined following Carnall et al. (2018), vs. the global formation timescale defined as the ratio of the age of the universe when 50% of the total stellar mass is formed to the age of the universe at the redshift of observation. The global and central SFHs of all galaxies are plotted in the smaller panels. The portions of SFH that are used to define  $\tau_{\text{center}}$  are highlighted with blue, black, and red. The vertical dashed lines in the right panels show the global measurement of  $t_{50}$  (i.e., the x-axis in the left panel). Quiescent galaxies that form their inner core more slowly (higher on the y-axis, left panel) are also formed earlier in the universe (to the right on the x-axis, left panel) and vice versa.

are formed later in the universe are forming their inner cores faster and have a younger center in general. The existence of fast/slow quenching channels is generally consistent with the unresolved observational studies of quiescent galaxies (e.g., Belli et al. 2019), but our spatially resolved study confirms it for the inner core and it supports the idea that the fast quenching channel should lead to age gradients. The existence of age gradients in quiescent galaxies is also broadly consistent with cosmological simulations (e.g., Wellons et al. 2015; Tacchella et al. 2016).

Consistent with Belli et al. (2019), we speculate that gas-rich mergers are potentially one of the mechanisms driving fast formation. We test this by using a sample of massive galaxies at  $z=2$  selected from the Illustris cosmological simulations (Genel et al. 2014; Vogelsberger et al. 2014a, 2014b; Nelson et al. 2015). Further details of this selection are described in Appendix B and Akhshik et al. (2020). We identify 23 galaxies that are 0.3 dex above the SFMS in the redshift range  $z=2-4$  with a prominent peak in their SFH corresponding to a starburst event. A starburst timescale is then measured by finding the difference between when this peak occurs and when the SFR decreases at least 0.6 dex below that maximum. This timescale is indeed short with an average of 250 Myr for 23 selected galaxies, and 18 out of these 23 galaxies have a timescale shorter than 400 Myr. Gas-rich mergers that can drive starburst events in star-forming galaxies are therefore largely short-lived within these simulations. While gas-rich mergers are not consistent with early slow-forming galaxies, they may be associated with fast forming galaxies (e.g., Belli et al. 2019; Tacchella et al. 2022).

We show that the quiescent galaxies that form later in the universe build up their cores faster and vice versa. At face value, this result is in tension with previous chemical abundance analyses that imply the opposite (e.g., Thomas et al. 2005). Our observations challenge the current paradigm where the earliest massive galaxies form most rapidly. However, the chemical abundance analyses of local early-type galaxies in Thomas et al. (2005) that support the current framework are unresolved and naturally probe long timescales owing to the epoch of observation. Over 10 billion years, dynamical processes could in principle homogenize the central formation timescale between  $z\sim 2$  and  $z\sim 0$  and effectively wash out the signatures that we capture at high redshift. Our observations could be consistent with a physical picture in which  $z\sim 2$  quiescent galaxies are formed via two different channels: central starbursts often triggered by gas-rich mergers at  $z\sim 2-4$  and gradual, accretion-throttled formation at early cosmic times when the universe was denser (Wellons et al. 2015). Future spatially resolved chemical abundance studies of galaxies closer to the epoch of formation at  $z\gtrsim 2$  with higher spectral resolution, potentially with the James Webb Space Telescope, are necessary to understand the origin of this tension. Our understanding of how massive galaxies formed the bulk of their stars thus may be incomplete and/or incorrect.

We finally note that the correlation between  $\tau_{\text{center}}$  and  $t(t_{50}^{\text{global}})$  does not trivially hold as the measured timescales in principle represent different properties of the SFHs.  $\tau_{\text{center}}$  measures the time difference between forming 50% of the stellar mass and when the SFR drops to 10% of its average,  $t_{\text{quench}}$ , normalized by  $t(t_{\text{quench}})$  for the center, whereas  $t(t_{50}^{\text{global}})$  measures the age of the universe when 50% of the global stellar mass is formed. For example, we have two galaxies in the

sample, MRG-M1341 and MRG-S1522, with almost the same  $t(t_{50}^{\text{global}})/t_{\text{univ}}$  but very different quenching timescales at their centers. As is clear from Figure 7, they also have distinct SFHs at their centers while having pretty similar global SFHs. However, we acknowledge that a sample of eight is not adequate to sample the full parameter space possible in this diagnostic plot. More data of similar quality would help build a more representative picture of central quenching relative to global formation timescales for the overall quiescent population at cosmic noon.

## 6. Summary

In this paper, we present the novel analysis of deep 5–15 orbit grism spectroscopy from the REQUIEM-2D survey of eight strongly lensed quiescent galaxies ranging from  $z=1.59$  to  $z=2.92$ . By combining the grism spectroscopy with HST and Spitzer imaging, we perform a spatially resolved spectrophotometric analysis, developing and publicly releasing the `requiem2d` software package. With this methodology, we can robustly constrain the star formation histories in the inner cores of distant galaxies in order to constrain signatures of formation and quenching. Our conclusions from this analysis are detailed as follows.

1. The REQUIEM-2D galaxies are not dusty ( $A_V < 1$ ) and have attenuation curves that are steeper than the Calzetti et al. (2000) law in the UV and flatter in the IR. We cannot reject flat metallicity gradients in the REQUIEM-2D survey.
2. Despite having only eight targets in the REQUIEM-2D survey, we already observe a diversity of formation pathways.
3. Our measurements only include the five central bins (Section 3 and Figure 2), sensitive to the inner  $\sim 1-2$  kpc of the galaxy cores. For these bins, corresponding to different radial distances given the morphology and gravitational magnification (see the  $x$ -axis in Figure 6), we have MRG-M0138 and MRG-S0851 with flat age gradients in their inner core, consistent with an early and almost spatially uniform formation scenario (Akhshik et al. 2020). The flat age gradients in these galaxies are consistent with the results of Jafariyazani et al. (2020) and Setton et al. (2020). We speculate that if there was a gradient at some point during their evolution in the inner half-light radius, it has since diminished, for example as a result of mergers. MRG-M1341 has a flat age gradient, too, but its formation pathway seems different, as the SFH implies an inside-out quenching (e.g., Wellons et al. 2015; Tacchella et al. 2016; Nelson et al. 2021).
4. We detect a statistically significant age gradient in MRG-S1522 at a  $\gtrsim 2.5\sigma$  level with  $z$ -scores of the age differences between the center and outermost bins being 2.7 and 2.9, respectively (Figure 5(e)). This galaxy looks younger in the inner half-light radius. This result is consistent with Gobat et al. (2017), and it may imply nonuniform quenching (Wellons et al. 2015). The recovered SFH of MRG-S1522 clearly indicates that this galaxy quenches in the outer bins first.
5. For the remaining four REQUIEM-2D galaxies, we find non-axisymmetric age gradients. Similar asymmetries are reported for both local and high-redshift galaxies (e.g., Li et al. 2015; Setton et al. 2020). While this asymmetry

may have significant implications for quenching, we note that by combining data points azimuthally, it washes out any statistically significant gradients. We also note that some massive rotationally supported star-forming galaxies at  $z \sim 2$  show slight disturbances in their morphology (Girard et al. 2018).

6. While the combined age gradients for the REQUIEM-2D sample are consistent with younger stellar populations in the inner half-light radius, only one galaxy (MRG-S1522) samples the age beyond the half-light radius. A larger sample with more independent data points at or beyond the half-light radius is required to reach a robust conclusion. This trend in combined age gradients is driven by only a single galaxy, MRG-S1522, which further supports the necessity of a larger sample to provide stronger evidence.
7. By investigating the age gradient patterns, the global formation timescales, and quenching timescales at the center, we conclude that the REQUIEM-2D galaxies that are forming their inner cores slowly and uniformly are consistent with an early formation scenario, whereas the galaxies that are forming their inner half-light radius faster are younger at the center and are generally formed later in the universe.
8. Our main result is in tension with previous unresolved chemical abundance analyses of local early-type galaxies (e.g., Thomas et al. 2005), supporting the current paradigm where the earliest massive galaxies form most rapidly. While dynamical processes can alleviate this tension, future spatially resolved chemical abundance studies closer to the epoch of formation with higher spectral resolution are necessary to understand its origin.

Future observations of lensed quiescent galaxies with high spatial and spectral resolution, such as those possible with the James Webb Space Telescope, can provide further insights into the metallicity, age, and chemical abundance gradients in the quiescent population to better constrain their formation pathways. For example, using NIRSpec/IFU, one should be able to constrain metallicity gradients because of NIRSpec’s superior spectral resolution relative to the G141 grism spectroscopy used herein. Also, by using the IFU, one can avoid the complications of the contamination by nearby objects in grism spectroscopy. This analysis serves as a jumping-off point, proposing a new diagnostic of formation pathways (i.e., Figure 7) that can be tested with larger samples, requiring high spatial resolution and a large enough signal-to-noise ratio in the outskirts of galaxies.

M.A. gratefully acknowledges support by NASA under award No 80NSSC19K1418. This work is based on observations made with the NASA/ESA Hubble Space Telescope, obtained at the Space Telescope Science Institute, which is operated by the Association of Universities for Research in Astronomy, Inc., under NASA contract NAS 5-26555. M.A. gratefully acknowledges support from STScI grants GO-14622 and GO-15633. K.W. wishes to acknowledge funding from the Alfred P. Sloan Foundation. S.T. and G.B. acknowledge support from the ERC Consolidator Grant funding scheme (project ConTExt, grant number No. 648179). The Cosmic Dawn Center is funded by the Danish National Research Foundation under grant No. 140. The Dunlap Institute is funded through an endowment established by the David

Dunlap family and the University of Toronto. G.M. acknowledges funding from the European Union’s Horizon 2020 research and innovation program under the Marie Skłodowska-Curie grant agreement No MARACHAS—DLV-896778. H.E. gratefully acknowledges support from STScI grant GO-15466. C.C.W. acknowledges support from NIRCcam Development Contract NAS5-02105 from NASA Goddard Space Flight Center to the University of Arizona.

## Appendix A Gravitational Lensing Model

MRG-P0918 is a highly magnified, singly imaged galaxy lensed by the massive galaxy cluster PSZ1 G295.24-21.55 at  $z = 0.61$  (Planck Collaboration et al. 2014). We make use of the HST images to locate three multiply lensed systems (numbered 1–3), composed of three images each. We present these multiple images in Table 2, adopting the usual notation  $X$ .  $Y$  where  $X$  identifies a system of multiple images and  $Y$  is a running number identifying all images for a given system. System 1 has a known spectroscopic redshift with  $z = 2.146$ . This redshift is measured using Grizli and its automated redshift fitting pipeline leveraging grism spectroscopy (observed as a part of HST-GO-15663). In particular, the [O III] doublet at rest-frame wavelengths of 4960/5008 Å is used to constrain the redshift with a reduced  $\chi^2$  of 1.04. However, systems 2 and 3 have unknown redshifts.

We model the mass distribution of PSZ1 G295.24-21.55 using the latest version (v7.1) of the public LENSTOOL software<sup>31</sup> (Jullo et al. 2007). Following previous work on cluster lens models (e.g., Richard et al. 2014), we assume the total mass distribution to be a combination of double pseudo-isothermal elliptical mass (dPIE) profiles parameterized with a velocity dispersion  $\sigma^*$ , a core radius  $r_{\text{core}}$ , and a cut radius  $r_{\text{cut}}$  (Suyu & Halkola 2010). The HST images show that the cluster is dominated by a central brightest cluster galaxy, and we therefore model the smooth cluster-scale mass distribution using a single dPIE mass distribution. Galaxy-scale mass components are added as individual dPIE profiles, where we select galaxies based on the cluster red sequence from HST color F555W – F814W. To reduce the number of parameters following previous works (e.g., Richard et al. 2010), we assume that the mass component parameters associated with the cluster members follow a scaling relation with respect to  $\sigma^*$  and  $r_{\text{cut}}^*$  for an  $L^*$  galaxy. We fix  $r_{\text{cut}}^* = 45$  kpc to remove degeneracy between these parameters. This does not affect the predictions from the lens model for MRG-P0918.

LENSTOOL uses a Monte Carlo Markov Chain (MCMC) to sample the posterior probability distribution of the model, expressed as a function of the likelihood defined in Jullo et al. (2007). In practice, we minimize the distances in the image plane:

$$\chi^2 = \sum_{ij} \frac{\theta_{\text{obs}}^{(i,j)} - \theta_{\text{pred}}^{(i,j)}}{\sigma_{\text{pos}}^2}, \quad (\text{A1})$$

with  $\theta_{\text{obs}}^{(i,j)}$  and  $\theta_{\text{pred}}^{(i,j)}$  representing the observed and predicted vector positions of the multiple image  $j$  in system  $i$ , respectively. Furthermore,  $\sigma_{\text{pos}}$  is a global error on the position of all multiple images, which we fix at  $0''.5$ .

<sup>31</sup> Publicly available at: <https://git-cral.univ-lyon1.fr/lenstool/lenstool>.

**Table 2**  
List of Multiply Imaged Systems Used as Constraints in the MRG-P0918 Mass Model

ID	$\alpha$ (deg)	$\delta$ (deg)	$z_{\text{prior}}$	$z_{\text{model}}$
1.1	09:18:51.68	−81:03:18.50	2.146	
1.2	09:18:49.92	−81:03:10.51	2.146	
1.3	09:18:50.60	−81:02:32.93	2.146	
2.1	09:19:00.56	−81:03:10.22	[0.8–5.0]	$1.66 \pm 0.04$
2.2	09:18:59.95	−81:03:15.40		
2.3	09:18:58.98	−81:02:43.44		
3.1	09:18:49.70	−81:03:28.89	[0.8–5.0]	$1.87 \pm 0.05$
3.2	09:18:45.48	−81:03:01.81		
3.3	09:18:47.26	−81:02:47.12		

**Note.** From left to right: identification number for the multiple image, sky coordinates, and redshift constraints from spectroscopy. Redshifts with error bars are not constrained with spectroscopy and are predictions from our lens model.

**Table 3**  
Mass Model Parameters for MRG-P0918

Potential	$\Delta\alpha$ (arcsec)	$\Delta\delta$ (arcsec)	$e$	$\theta$ (deg)	$r_{\text{core}}$ (kpc)	$r_{\text{cut}}$ (kpc)	$\sigma$ (km s <sup>−1</sup> )
Dark Matter	$-5.0^{+0.9}_{-0.0}$	$-0.5^{+0.5}_{-0.3}$	$0.50^{+0.00}_{-0.01}$	$176.9^{+0.6}_{-0.4}$	$140^{+18}_{-10}$	[1000]	$1319^{+43}_{-25}$
$L^*$ galaxy					[0.15]	[45]	$127^{+7}_{-17}$

**Note.** The reference world coordinate system (WCS) location corresponds to the brightest cluster member (09:18:51.11, −81:03:04.35). From left to right: mass component, position relative to the cluster center ( $\Delta R.A.$  and  $\Delta \text{decl.}$ ), dPIE shape (ellipticity and orientation), core and cut radii, and velocity dispersion. The final row is the generic galaxy mass at the characteristic luminosity  $L^*$ , which is scaled to match each of the cluster member galaxies. Parameters in square brackets are fixed a priori in the model.

**Table 4**

The Values of the Linear Gravitational Magnification  $\mu$ , and the Source-plane Half-light Radius  $r_c$  Defined in Section 4

Target	$\mu$	$r_c$ (arcsec)
MRG-M1341	$30 \pm 8$	$0''.32 \pm 0''.04$
MRG-M0138	$13 \pm 5$	$0''.4 \pm 0''.1$
MRG-M0150	$5 \pm 1$	$0''.2 \pm 0''.03$
MRG-P0918	$7.7 \pm 0.9$	$0''.22 \pm 0''.01$
MRG-S1522	$15 \pm 6$	$0''.06 \pm 0''.01$
MRG-M2129	$4.6 \pm 0.2$	$0''.25 \pm 0''.01$
MRG-M0454	$11 \pm 2$	$0''.13 \pm 0''.01$

**Note.** The gravitational magnifications are from this appendix and Ebeling et al. (2018), Man et al. (2021), Newman et al. (2018), Rodney et al. (2021), and Sharon et al. (2020).

Using all three systems from Table 2 as constraints, we obtain a best-fit rms of  $1''.4$  for this mass model. The best-fit parameters for the mass distribution and the optimized redshifts of systems 2 and 3 are presented in Tables 3 and 2 respectively. Based on the best-fit mass model of the cluster, we predict a magnification of  $\mu = 7.69 \pm 0.86$  for MRG-P0918. We also summarize all the measured magnifications and half-light radii in Table 4.

## Appendix B Testing Our Methodology

In this Appendix, we discuss different tests we perform to demonstrate that the `requiem2d` age estimates are unbiased

and the uncertainties are realistic. We first summarize the tests performed in Akhshik et al. (2020), and we present a new test at the end.

We use the SFHs of galaxies at  $z = 2$  from the Illustris cosmological simulations (Genel et al. 2014; Vogelsberger et al. 2014a, 2014b; Nelson et al. 2015) to generate realistic mock observations as discussed in detail in Akhshik et al. (2020). A subsample of 71 simulated quiescent galaxies are then selected using the SFMS. For each SFH in the subsample, the MRG-S0851 morphology is subsequently used to generate a mock G141 grism spectrum, and we finally calculate the mock photometric observations in five HST bands of  $U_{\text{F390W}}$ ,  $I_{\text{F814W}}$ ,  $Y_{\text{F105W}}$ ,  $J_{\text{F125W}}$  and  $H_{\text{F160W}}$ , and Spitzer IRAC channels 1 and 2. For each one of the 71 mock galaxies, we randomly draw the grism noise level from a uniform distribution of 1%–10%, assuming the photometric noise is one-fifth of the grism noise.

Three tests are performed using the above mock observations in Akhshik et al. (2020), quantifying our ability to recover: (1) global SFHs and ages of both quiescent and star-forming galaxies, and (2) age gradients of quiescent galaxies. We were able to recover mock ages of the quiescent galaxies with minimal noticeable biases except for ages older than  $\sim 1.5$  Gyr, where the recovered ages are slightly younger. The estimates of the ages of star-forming galaxies showed no biases, potentially because of their younger ages in general. There were no significant biases in our estimates of the age gradient patterns. We note that the general trends in SFH are recovered reasonably well, even with cases that have multiple peaks of star formation or a few episodes of increasing and decreasing

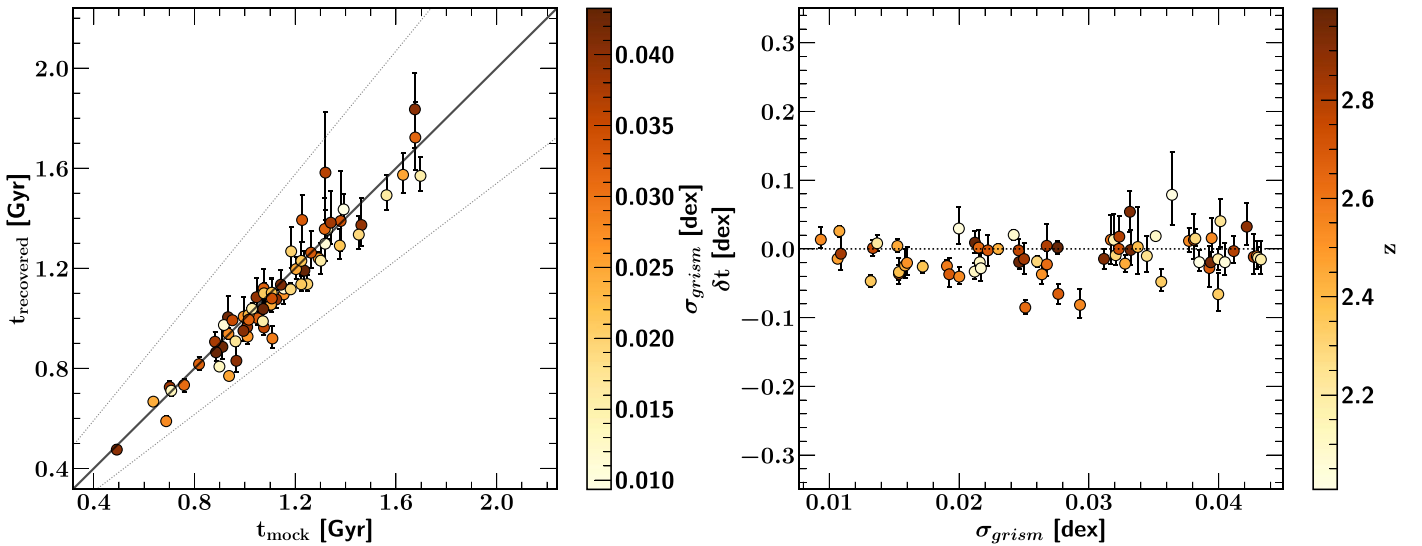


**Figure 8.** Testing our methodology to recover global SFHs and ages using a sample of massive quiescent galaxies selected from the Illustris simulation. Left panel: recovered vs. actual global  $t_{50}$  ages, color-coded by grism noise. The solid line is the one-to-one relation and the dotted lines are  $\pm 0.1$  dex scatter. Right panel: deviation of median recovered  $t_{50}$  ages from the true ages vs. grism noise, color-coded by mock redshift. No noticeable systematic biases can be seen, indicating that our choice of prior for SFHs reasonably recovers the ages of massive quiescent galaxies selected from the Illustris simulation.

SFH. However, one place our fit struggles is in recovering particularly stochastic jumps in the SFH that happen on shorter timescales (of the order of 100 Myr or less). This is potentially due to the continuity prior that disfavors sharp transitions in the SFH.

The redshifts of the quiescent galaxies in the tests performed in Akhshik et al. (2020) were fixed at  $z=2$ . However, the REQUIEM-2D galaxies span redshifts of  $z = 1.6$  to  $z = 2.9$ . This is potentially important because the WFC3/G141 grism can provide clean spectra usually in the observed 1.2–1.6  $\mu\text{m}$  wavelength range, and with changing redshifts, different age-sensitive features will be observed in the bandpass. For example, for a  $z=2$  target, we would be able to observe  $\text{H}\beta$ , but for a  $z=2.5$  target this feature is outside the bandpass, but we can observe  $\text{H}\gamma$ . As the largest impact on the G141 bandpass is at higher redshifts, we test the impact by using the same Illustris SFHs for 71 quiescent galaxies selected following Akhshik et al. (2020). However, we now additionally randomly draw and assign a redshift from a uniform distribution between  $z=2$  and  $z=3$ . We follow the same procedure to generate mock data and add noise.

The result of this test is shown in Figure 8. There are no noticeable systematic biases in the recovered ages, consistent with Akhshik et al. (2020). Therefore, we demonstrate that `requiem2d` can reliably recover the mock ages for quiescent

galaxies at  $z=2-3$  (with a variation of less than 0.1 dex). We also do not notice any biases in the recovered age estimates as we vary redshift (Figure 8, right panel). We conclude that for the redshifts of  $z=2-3$ , similar to the REQUIEM-2D galaxies, the `requiem2d` code should provide unbiased estimates of ages as validated using Illustris SFHs.

We finally note that using parametric as opposed to nonparametric SFH models can have a significant effect on the estimated parameters (e.g., Newman et al. 2018; Leja et al. 2019); the best-fit models for galaxies are usually older and more massive (Leja et al. 2019). We use nonparametric SFHs because the parametric SFHs, such as exponentially decaying functions, cannot adequately reproduce the SFHs we observe in the Illustris cosmological simulations—some simulated galaxies have more complex variations in their SFHs. This leads to biased estimates in the recovered stellar population parameters, as also discussed in Lower et al. (2020).

### Appendix C Joint Spectrophotometric Fit

We discussed the joint spectrophotometric fit in Section 4 and present the results for one of the targets, MRG-M1341, there (Figure 3). We show the similar plots for the rest of the targets here in Figures 9–14.



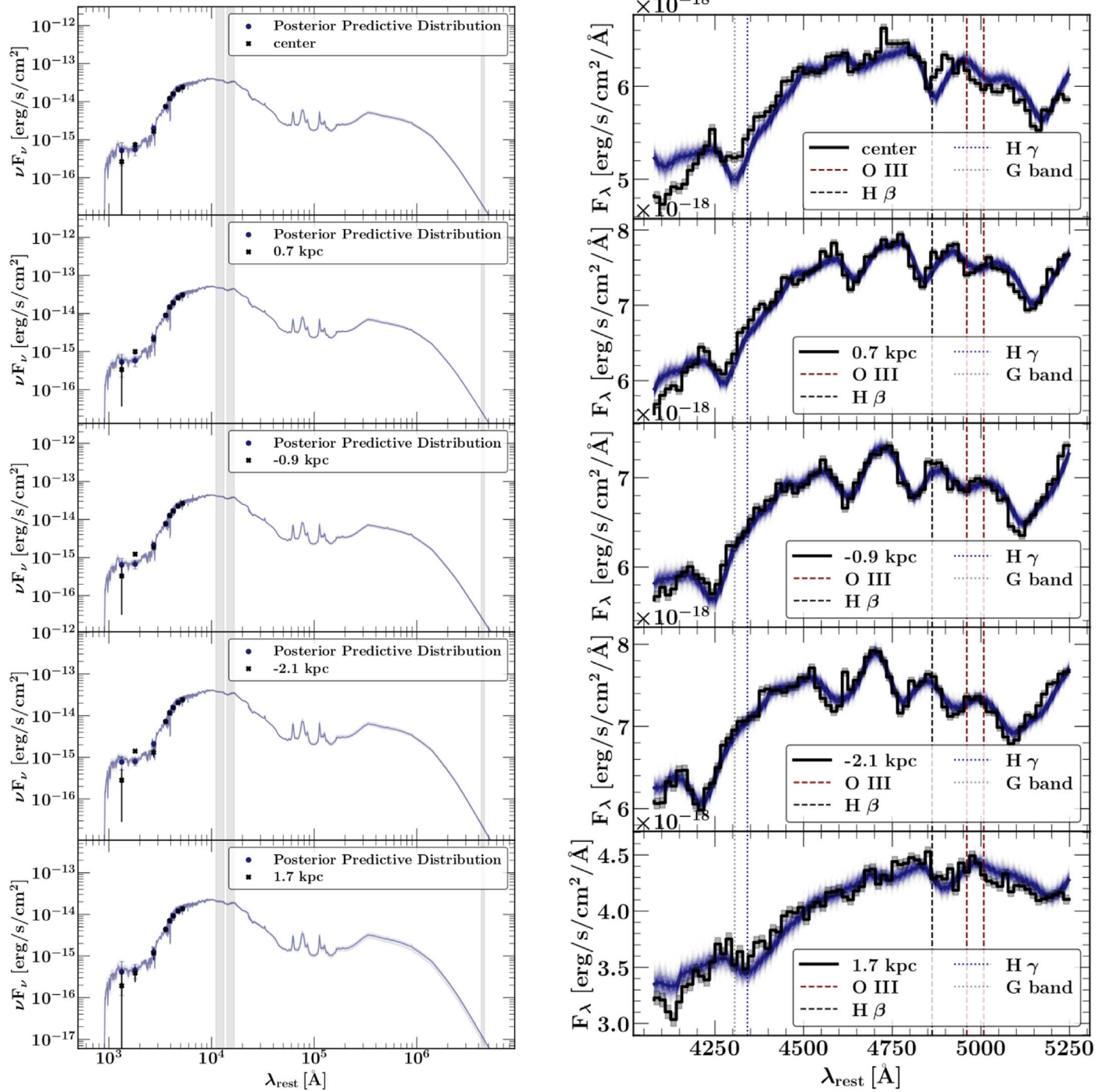


**Figure 9.** Left: the SED of MRG-M0138. The blue line shows 200 draws from the FSPS model. The shaded regions in the SED coincide with the bandpasses of the unresolved Spitzer IRAC channels 1 and 2 and semi-resolved ALMA 1.3 mm. Right: the resolved extracted 1D grism spectra.

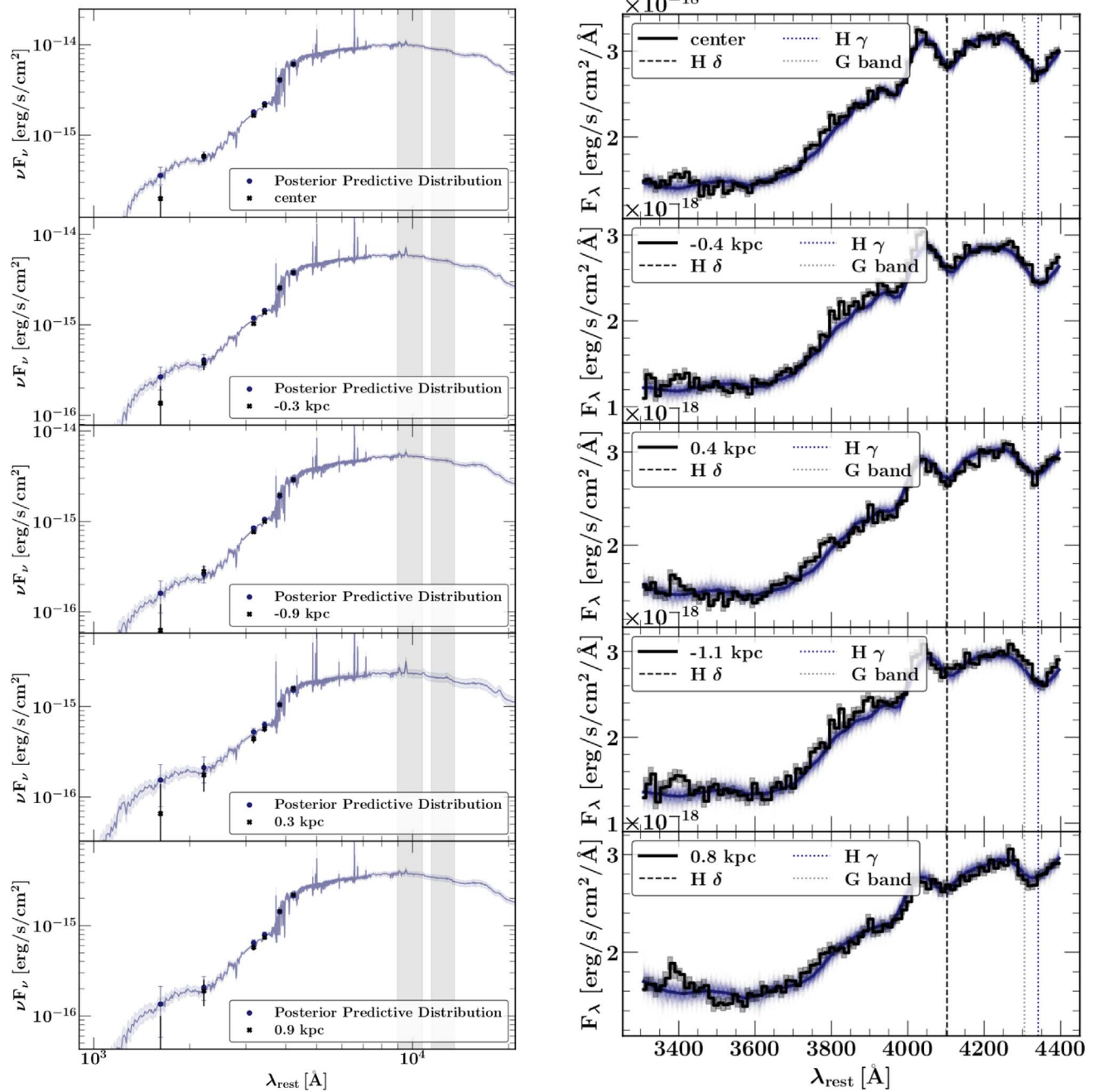


**Figure 10.** Left: the SED of MRG-M0150. The blue line shows 200 draws from the FSPS model. The shaded regions in the SED coincide with the bandpasses of the unresolved Spitzer IRAC channels 1 and 2. Right: the resolved extracted 1D grism spectra.

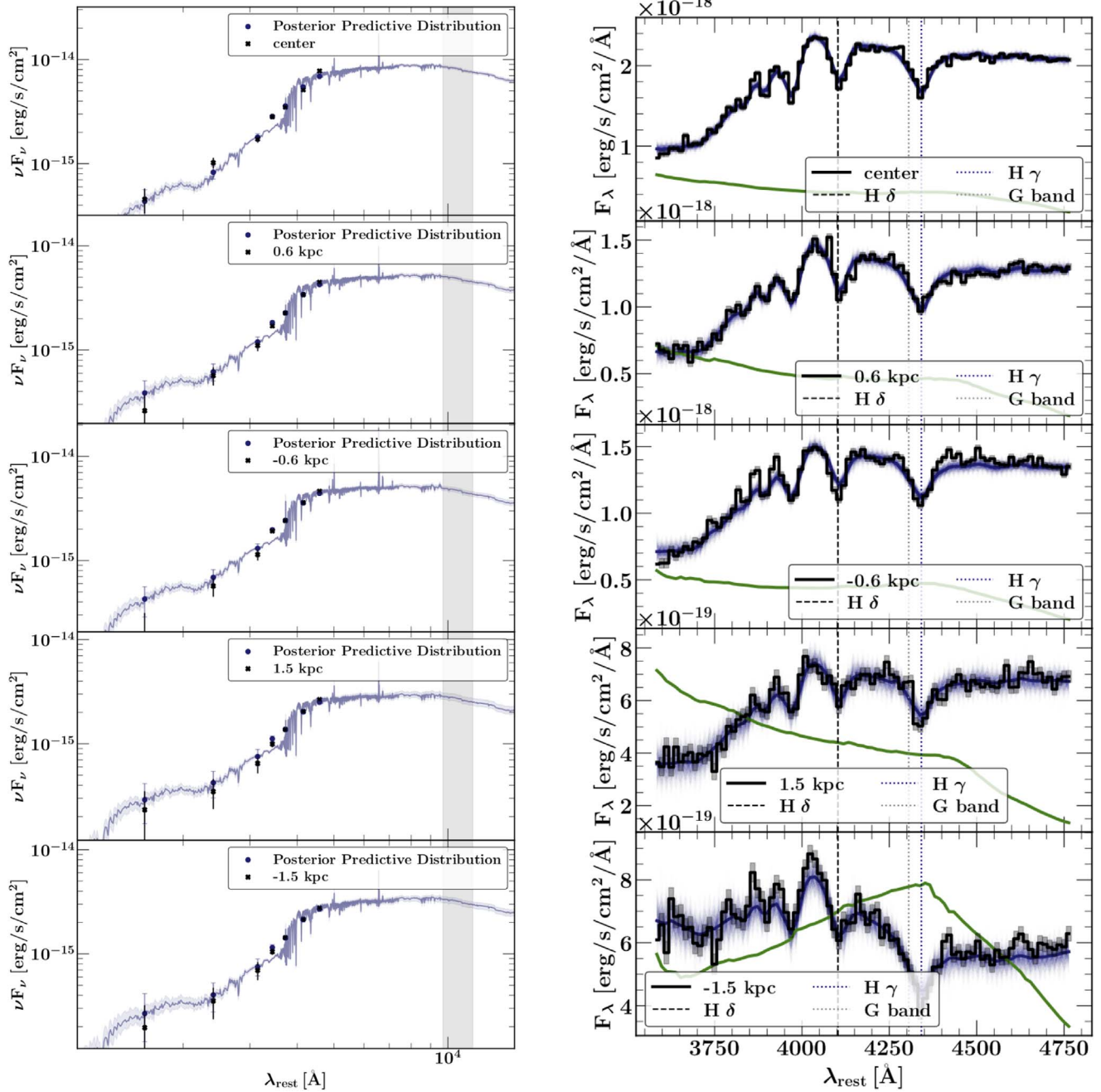


**Figure 11.** Left: the SED of MRG-P0918. The blue line shows 200 draws from the FSPS model. The shaded regions in the SED coincide with the bandpass of the unresolved Spitzer IRAC channel 1. Right: the resolved extracted 1D grism spectra. The green line in the spectra denotes the collapsed 1D contamination, affecting the shape of the spectra of the outer bins significantly.

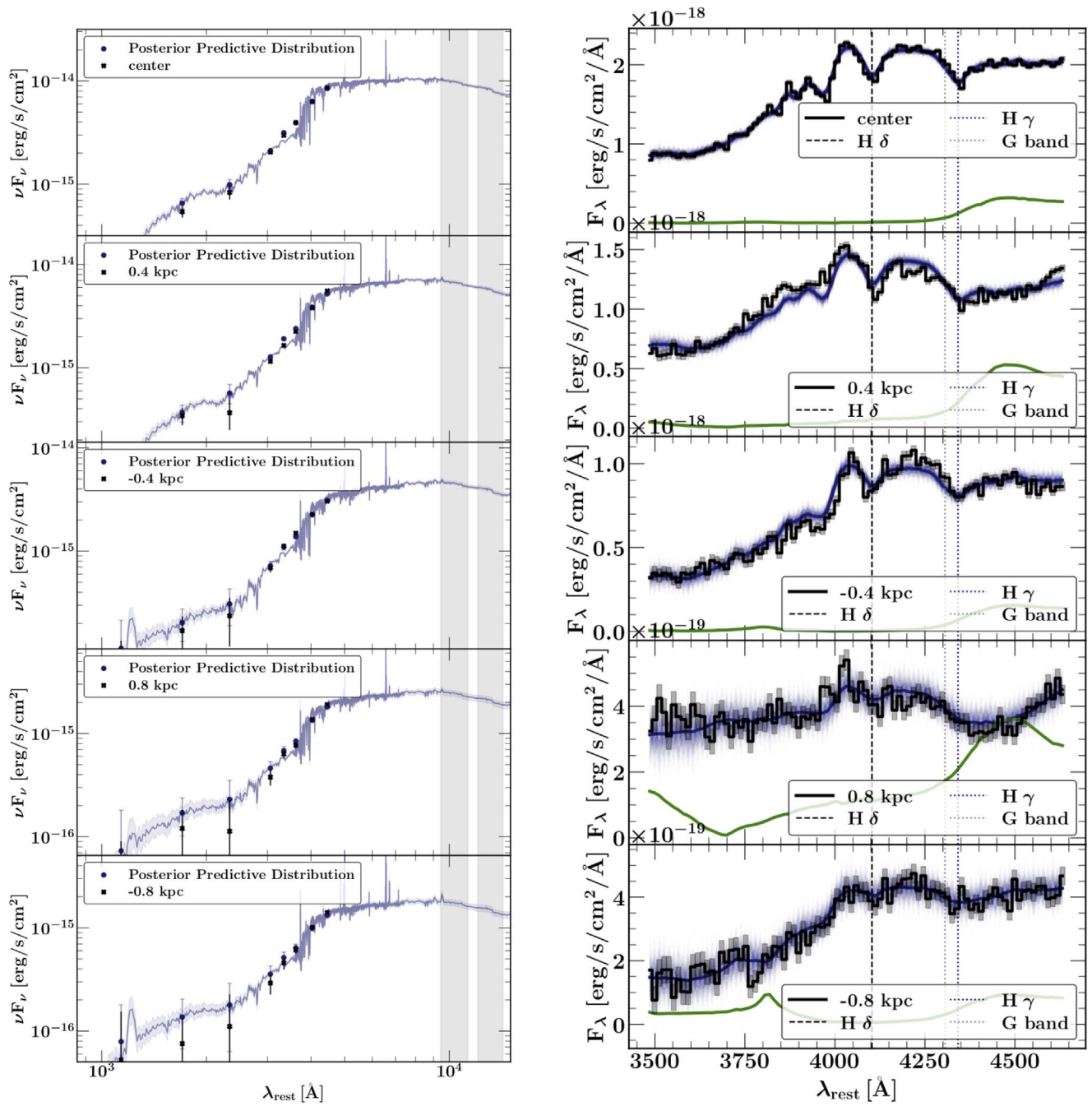


**Figure 12.** Left: the SED of MRG-S1522. The blue line shows 200 draws from the FSPS model. The shaded regions in the SED coincide with the bandpasses of the unresolving Spitzer IRAC channels 1 and 2. Right: the resolved extracted 1D grism spectra. The green line in the spectra denotes the collapsed 1D contamination, affecting the shape of the spectra of the outer bins significantly.

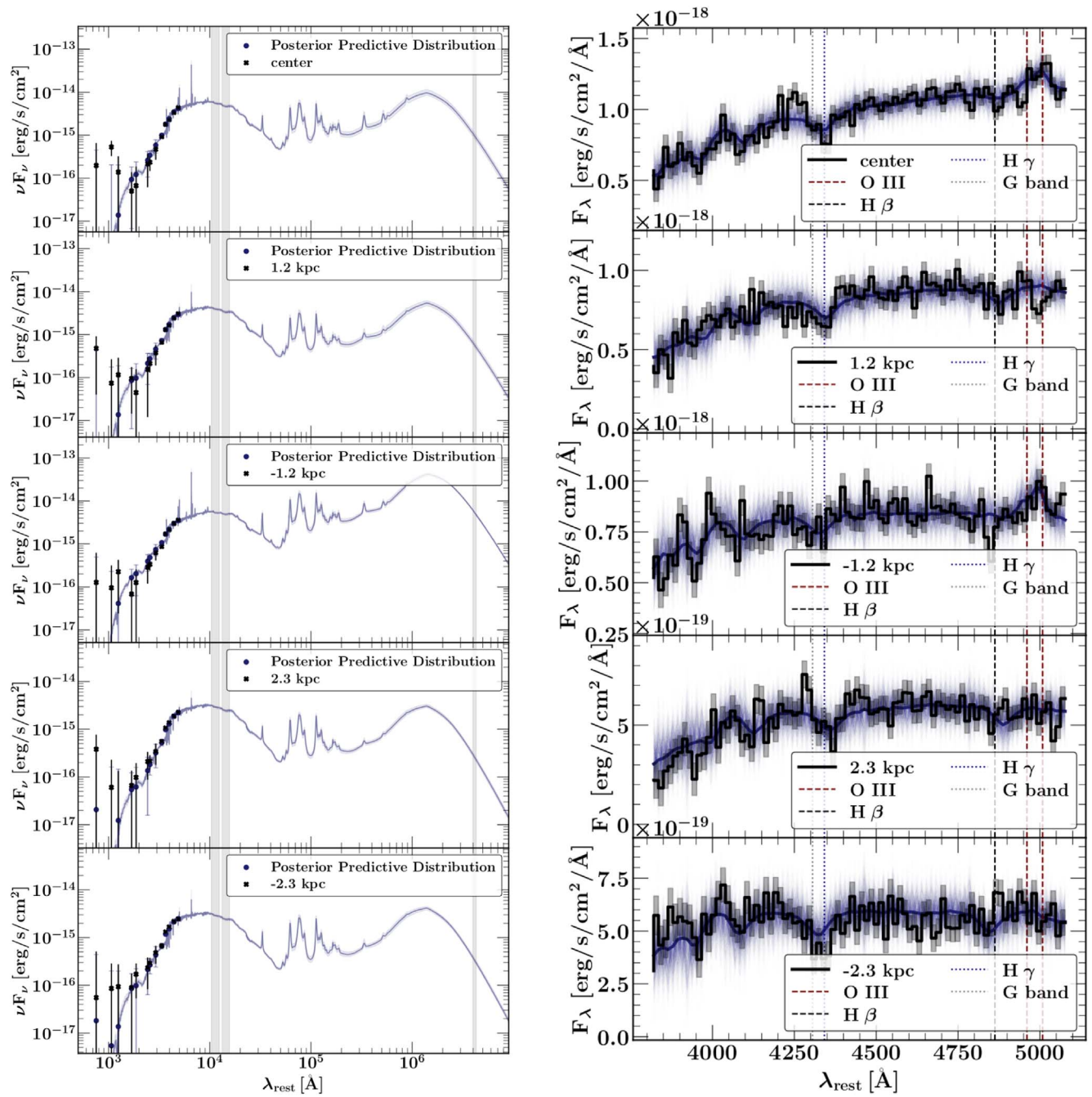


**Figure 13.** Left: the SED of MRG-M2129. The blue line shows 200 draws from the FSPS model. The shaded regions in the SED coincide with the bandpasses of the unresolved Spitzer IRAC channels 1 and 2 as well as ALMA 1.3 mm. Right: the resolved extracted 1D grism spectra.

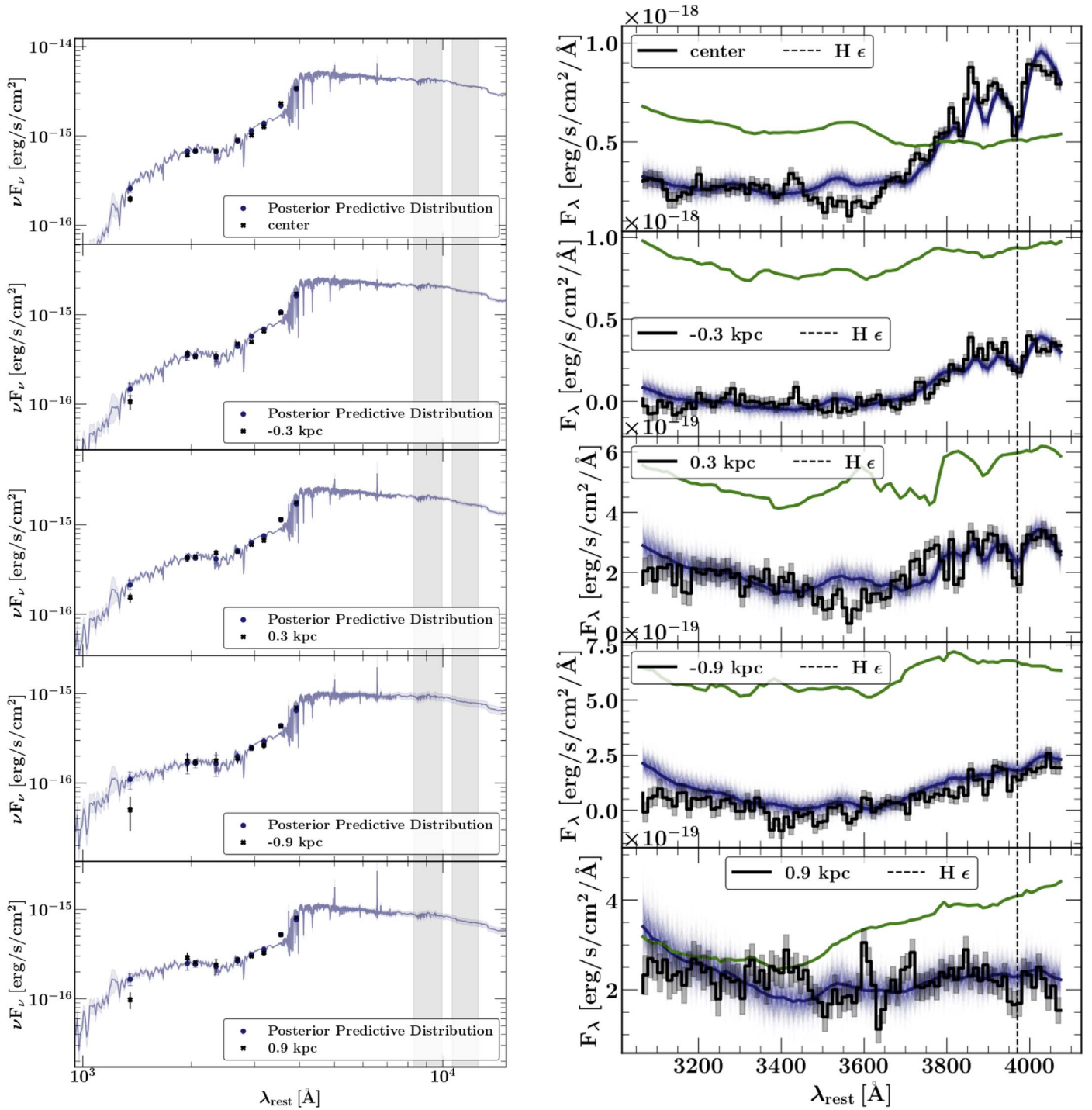


**Figure 14.** Left: the SED of MRG-M0454. The blue line shows 200 draws from the FSPS model. The shaded regions in the SED coincide with the unresolved Spitzer IRAC channels 1 and 2. Right: the resolved extracted 1D grism spectra. The green line in the spectra denotes the collapsed 1D contamination, affecting the shape of the spectra of all bins significantly.

## ORCID iDs

Mohammad Akshshik  <https://orcid.org/0000-0002-3240-7660>  
 Katherine E. Whitaker  <https://orcid.org/0000-0001-7160-3632>  
 Joel Leja  <https://orcid.org/0000-0001-6755-1315>  
 Johan Richard  <https://orcid.org/0000-0001-5492-1049>  
 Justin S. Spilker  <https://orcid.org/0000-0003-3256-5615>  
 Mimi Song  <https://orcid.org/0000-0002-8442-3128>  
 Gabriel Brammer  <https://orcid.org/0000-0003-2680-005X>  
 Rachel Bezanson  <https://orcid.org/0000-0001-5063-8254>  
 Harald Ebeling  <https://orcid.org/0000-0001-8249-2739>  
 Anna R. Gallazzi  <https://orcid.org/0000-0002-9656-1800>  
 Guillaume Mahler  <https://orcid.org/0000-0003-3266-2001>  
 Lamiya A. Mowla  <https://orcid.org/0000-0002-8530-9765>  
 Erica J. Nelson  <https://orcid.org/0000-0002-7524-374X>  
 Camilla Pacifici  <https://orcid.org/0000-0003-4196-0617>  
 Keren Sharon  <https://orcid.org/0000-0002-7559-0864>  
 Sune Toft  <https://orcid.org/0000-0003-3631-7176>  
 Christina C. Williams  <https://orcid.org/0000-0003-2919-7495>  
 Johannes Zabl  <https://orcid.org/0000-0002-9842-6354>

## References

- Abramson, L. E., Newman, A. B., Treu, T., et al. 2018, *AJ*, 156, 29  
 Akshshik, M., Whitaker, K. E., Brammer, G., et al. 2020, *ApJ*, 900, 184  
 Akshshik, M., Whitaker, K. E., Leja, J., et al. 2021, *ApJL*, 907, L8  
 Anderson, J. 2016, Empirical Models for the WFC3/IR PSF, Space Telescope WFC Instrument Science Report, 2016-12  
 Avila, R. J., & Hack, W. J. 2012, AAS Meeting, 220, 135.13  
 Belli, S., Contursi, A., Genzel, R., et al. 2021, *ApJL*, 909, L11  
 Belli, S., Genzel, R., Förster Schreiber, N. M., et al. 2017, *ApJL*, 841, L6  
 Belli, S., Newman, A. B., & Ellis, R. S. 2019, *ApJ*, 874, 17  
 Bertin, E., & Armouts, S. 1996, *A&AS*, 117, 393  
 Bezanson, R., Spilker, J., Williams, C. C., et al. 2019, *ApJL*, 873, L19  
 Brammer, G. 2016, Grizli: The Grism redshift & Line Database for HST WFC3/IR Spectroscopy, HST Proposal, 24, 14553  
 Brammer, G. B., Sánchez-Janssen, R., Labbé, I., et al. 2012, *ApJL*, 758, L17  
 Brammer, G. B., Whitaker, K. E., van Dokkum, P. G., et al. 2009, *ApJL*, 706, L173  
 Caliendo, J. N., Whitaker, K. E., Akshshik, M., et al. 2021, *ApJL*, 910, L7  
 Calzetti, D., Armus, L., Bohlin, R. C., et al. 2000, *ApJ*, 533, 682  
 Carnall, A. C., McLure, R. J., Dunlop, J. S., & Davé, R. 2018, *MNRAS*, 480, 4379  
 Cassata, P., Gialalisco, M., Williams, C. C., et al. 2013, *ApJ*, 775, 106  
 Chabrier, G. 2003, *PASP*, 115, 763  
 Conroy, C., & Gunn, J. E. 2010, FSPS: Flexible Stellar Population Synthesis, Astrophysics Source Code Library, ascl:1010.043  
 Conroy, C., Gunn, J. E., & White, M. 2009, *ApJ*, 699, 486  
 Daddi, E., Dickinson, M., Morrison, G., et al. 2007, *ApJ*, 670, 156  
 Dekel, A., & Birnboim, Y. 2006, *MNRAS*, 368, 2  
 Ebeling, H., Stockmann, M., Richard, J., et al. 2018, *ApJ*, 852, L7  
 Elbaz, D., Daddi, E., Le Borgne, D., et al. 2007, *A&A*, 468, 33  
 Estrada-Carpenter, V., Papovich, C., Momcheva, I., et al. 2019, *ApJ*, 870, 133  
 Estrada-Carpenter, V., Papovich, C., Momcheva, I., et al. 2020, *ApJ*, 898, 171  
 Flewelling, H. A., Magnier, E. A., Chambers, K. C., et al. 2020, *ApJS*, 251, 7  
 Gaia Collaboration, Brown, A. G. A., Vallenari, A., et al. 2018, *A&A*, 616, A1  
 Geier, S., Richard, J., Man, A. W. S., et al. 2013, *ApJ*, 777, 87  
 Gelman, A., & Rubin, D. B. 1992, *StatSci*, 7, 457  
 Genel, S., Vogelsberger, M., Springel, V., et al. 2014, *MNRAS*, 445, 175  
 Girard, M., Dessauges-Zavadsky, M., Schaerer, D., et al. 2018, *A&A*, 613, A72  
 Gobat, R., Daddi, E., Strazzullo, V., et al. 2017, *A&A*, 599, A95  
 Hill, A. R., Muzzin, A., Franx, M., & van de Sande, J. 2016, *ApJ*, 819, 74  
 Homan, M. D., & Gelman, A. 2014, J. Mach. Learn. Res., 15, 1593, <http://jmlr.org/papers/v15/hoffman14a.html>  
 Horne, K. 1986, *PASP*, 98, 609  
 Jafariyazani, M., Newman, A. B., Mobasher, B., et al. 2020, *ApJL*, 897, L42  
 Jauzac, M., Klein, B., Kneib, J.-P., et al. 2021, *MNRAS*, 508, 1206  
 Johnson, B. D., Leja, J. L., Conroy, C., & Speagle, J. S. 2019, Prospector: Stellar population inference from spectra and SEDs, ascl:1905.025  
 Jullo, E., Kneib, J. P., Limousin, M., et al. 2007, *NJPh*, 9, 447  
 Kelson, D. D. 2014, arXiv:1406.5191  
 Kriek, M., & Conroy, C. 2013, *ApJ*, 775, L16  
 Kriek, M., van Dokkum, P. G., Franx, M., et al. 2006, *ApJL*, 649, L71  
 Leja, J., Johnson, B. D., Conroy, C., et al. 2019, *ApJ*, 877, 140  
 Leja, J., Johnson, B. D., Conroy, C., et al. 2020, in IAU Symp. 352, Uncovering Early Galaxy Evolution in the ALMA and JWST Era, ed. E. da Cunha et al. (Cambridge: Cambridge Univ. Press), 99  
 Leja, J., Johnson, B. D., Conroy, C., van Dokkum, P. G., & Byler, N. 2017, *ApJ*, 837, 170  
 Leja, J., Speagle, J. S., Ting, Y.-S., et al. 2022, *ApJ*, 936, 165  
 Li, C., Wang, E., Lin, L., et al. 2015, *ApJ*, 804, 125  
 Lindegren, L., Hernández, J., Bombrun, A., et al. 2018, *A&A*, 616, A2  
 Lower, S., Narayanan, D., Leja, J., et al. 2020, *ApJ*, 904, 33  
 Man, A. W. S., Zabl, J., Brammer, G. B., et al. 2021, *ApJ*, 919, 20  
 Momcheva, I. G., Brammer, G. B., van Dokkum, P. G., et al. 2016, *ApJS*, 225, 27  
 Morishita, T., Abramson, L. E., Treu, T., et al. 2018, *ApJL*, 856, L4  
 Morishita, T., Abramson, L. E., Treu, T., et al. 2019, *ApJ*, 877, 141  
 Muzzin, A., Marchesini, D., Stefanon, M., et al. 2013, *ApJ*, 777, 18  
 Nelson, D., Pillepich, A., Genel, S., et al. 2015, *A&C*, 13, 12  
 Nelson, E. J., Tacchella, S., Diemer, B., et al. 2021, *MNRAS*, 508, 219  
 Newman, A. B., Belli, S., & Ellis, R. S. 2015, *ApJ*, 813, L7  
 Newman, A. B., Belli, S., Ellis, R. S., & Patel, S. G. 2018, *ApJ*, 862, 125  
 Noeske, K. G., Faber, S. M., Weiner, B. J., et al. 2007, *ApJL*, 660, L47  
 Noll, S., Pierini, D., Cimatti, A., et al. 2009, *A&A*, 499, 69  
 Peng, C. Y., Ho, L. C., Impey, C. D., & Rix, H.-W. 2011, GALFIT: Detailed Structural Decomposition of Galaxy Images, Astrophysics Source Code Library, ascl:1104.010  
 Planck Collaboration, Ade, P. A. R., Aghanim, N., et al. 2014, *A&A*, 571, A29  
 Richard, J., Jauzac, M., Limousin, M., et al. 2014, *MNRAS*, 444, 268  
 Richard, J., Smith, G. P., Kneib, J.-P., et al. 2010, *MNRAS*, 404, 325  
 Rodney, S. A., Brammer, G. B., Pierel, J. D. R., et al. 2021, *NatAs*, 5, 1118  
 Salim, S., Boquien, M., & Lee, J. C. 2018, *ApJ*, 859, 11  
 Salvatier, J., Wiecki, T. V., & Fonnesbeck, C. 2016, PeerJ PrePrints, 4, e1686, <https://dblp.uni-trier.de/db/journals/peerjpre/peerjpre4.html#SalvatierWF16>  
 Setton, D. J., Bezanson, R., Suess, K. A., et al. 2020, *ApJ*, 905, 79  
 Sharon, K., Bayliss, M. B., Dahle, H., et al. 2020, *ApJS*, 247, 12  
 Skelton, R. E., Whitaker, K. E., Momcheva, I. G., et al. 2014, *ApJS*, 214, 24  
 Speagle, J. S., Steinhardt, C. L., Capak, P. L., & Silverman, J. D. 2014, *ApJS*, 214, 15  
 Spilker, J., Bezanson, R., Barišić, I., et al. 2018, *ApJ*, 860, 103  
 2020, Stan Development Team: Stan: the R interface to Stan, r package v2.21.2, <http://mc-stan.org/>  
 Suess, K. A., Bezanson, R., Spilker, J. S., et al. 2017, *ApJL*, 846, L14  
 Suyu, S. H., & Halkola, A. 2010, *A&A*, 524, A94  
 Tacchella, S., Carollo, C. M., Renzini, A., et al. 2015, *Sci*, 348, 314  
 Tacchella, S., Conroy, C., Faber, S. M., et al. 2022, *ApJ*, 926, 134  
 Tacchella, S., Dekel, A., Carollo, C. M., et al. 2016, *MNRAS*, 458, 242  
 Thomas, D., Maraston, C., Bender, R., & Mendes de Oliveira, C. 2005, *ApJ*, 621, 673  
 Toft, S., Zabl, J., Richard, J., et al. 2017, *Natur*, 546, 510  
 Umetsu, K., Medezinski, E., Nonino, M., et al. 2014, *ApJ*, 795, 163  
 Vogelsberger, M., Genel, S., Springel, V., et al. 2014a, *MNRAS*, 444, 1518  
 Vogelsberger, M., Genel, S., Springel, V., et al. 2014b, *Natur*, 509, 177  
 Wellons, S., Torrey, P., Ma, C.-P., et al. 2015, *MNRAS*, 449, 361  
 Whitaker, K., Capak, P., Davidzon, I., et al. 2019, Resolving QUIEscent Magnified (REQUIEM) Galaxies: The Missing (Spitzer/IRAC) Piece of the Puzzle, Spitzer Proposal, 14250  
 Whitaker, K. E., Franx, M., Leja, J., et al. 2014, *ApJ*, 795, 104  
 Whitaker, K. E., Labbé, I., van Dokkum, P. G., et al. 2011, *ApJ*, 735, 86  
 Whitaker, K. E., van Dokkum, P. G., Brammer, G., et al. 2013, *ApJL*, 770, L39  
 Whitaker, K. E., van Dokkum, P. G., Brammer, G., & Franx, M. 2012, *ApJL*, 754, L29  
 Whitaker, K. E., Williams, C. C., Mowla, L., et al. 2021, *Natur*, 597, 485  
 Williams, C. C., Gialalisco, M., Cassata, P., et al. 2014, *ApJ*, 780, 1

Williams, C. C., Spilker, J. S., Whitaker, K. E., et al. 2021, [ApJ](#), 908, 54  
Wisnioski, E., Förster Schreiber, N. M., Wuyts, S., et al. 2015, [ApJ](#), 799, 209  
Wuyts, E., Barrientos, L. F., Gladders, M. D., et al. 2010, [ApJ](#), 724, 1182

Zalesky, L., & Ebeling, H. 2020, [MNRAS](#), 498, 1121  
Zitrin, A., Zheng, W., Broadhurst, T., et al. 2014, [ApJL](#), 793, L12  
Zolotov, A., Dekel, A., Mandelker, N., et al. 2015, [MNRAS](#), 450, 2327